# Entanglement and classical fluctuations at finite-temperature critical points

## Sascha Wald[1], Raúl Arias[1,2] and Vincenzo Alba[3,4]

[1] SISSA and INFN, via Bonomea 265, 34136 Trieste, Italy
[2] Instituto de Física La Plata—CONICET and Departamento de Física, Universidad Nacional de La Plata C.C. 67, 1900, La Plata, Argentina
[3] Institute for Theoretical Physics, Universiteit van Amsterdam, Science Park 904, Postbus 94485, 1098 XH Amsterdam, The Netherlands
E-mail: v.alba@uva.nl

**Abstract.** We investigate several entanglement-related quantities at finite-temperature criticality in the three-dimensional quantum spherical model, both as a function of temperature $T$ and of the quantum parameter $g$, which measures the strength of quantum fluctuations. While the von Neumann and the Rényi entropies exhibit a volume-law for any $g$ and $T$, the mutual information obeys an area law. The prefactors of the volume-law and of the area-law are regular across the transition, reflecting that universal singular terms vanish at the transition. This implies that the mutual information is dominated by nonuniversal contributions. This hampers its use as a witness of criticality, at least in the spherical model. We also study the logarithmic negativity. For any value of $g$, $T$, the negativity exhibits an area-law. The negativity vanishes deep in the paramagnetic phase, it is larger at small temperature, and it decreases upon increasing the temperature. For any $g$, it exhibits the so-called sudden death, i.e. it is exactly zero for large enough $T$. The vanishing of the negativity defines a 'death line', which we characterise analytically at small $g$. Importantly, for any finite $T$ the area-law prefactor is regular across the transition, whereas it develops a cusp-like singularity in the limit $T \to 0$. Finally, we consider the single-particle entanglement and negativity spectra. The vast majority of the levels are regular across the transition. Only the larger ones exhibit singularities. These are related to the presence of a zero mode, which reflects the symmetry breaking. This implies the presence of sub-leading

[4] Author to whom any correspondence should be addressed.

singular terms in the entanglement entropies. Interestingly, since the larger levels do not contribute to the negativity, sub-leading singular corrections are expected to be suppressed for the negativity.

## Contents

*J. Stat. Mech.* (2020) 033105

## 1. Introduction

Understanding the interplay between entanglement and classical fluctuations in quantum many-body systems is a challenging task. Several entanglement-related quantities have been investigated [1–4]. Arguably, the most popular ones are the Rényi entropies and the von Neumann entropy. Given a partition of the system in subsystems $A$ and its complement $B \equiv \bar{A}$ (see figure 1(a) for a three-dimensional (3D) setup), the Rényi entropies $S_n$ are defined as

$$S_n \equiv \frac{1}{1-n} \ln \text{Tr} \rho_A^n, \tag{1}$$

with $\rho_A$ the reduced density matrix of part $A$. In the limit $n \to 1$ one obtains the so-called von Neumann entropy $S = -\text{Tr} \rho_A \ln \rho_A$. If the total system $A \cup \bar{A}$ is in a pure state, $S_n$ are good measures of the entanglement between $A$ and $B$. At zero temperature the famous area-law behaviour $S_n \propto L^{d-1}$ holds true, with $L$ being the linear size of the system, and $d$ the dimensionality. Logarithmic corrections are present for gapless fermionic systems [5–7]. This is strikingly different at finite temperature, where $S_n$ cannot distinguish genuine quantum correlations from thermal ones. At finite temperature the volume-law behaviour $S_n \propto L^d$ holds, reflecting, for instance, the transformation between entanglement and standard thermodynamic entropy. In this situation, the mutual information $I_{n,A:\bar{A}}$ (see section 2 for its definition) can be used to measure the total correlation, i.e. both classical and quantum, between $A$ and $\bar{A}$. The mutual information exhibits the area-law behaviour $I_n \propto L^{d-1}$. Still, $I_n$ is not a proper measure of the mutual entanglement between $A$ and $\bar{A}$. This reflects $A \cup \bar{A}$ being in a mixed state. The so-called logarithmic negativity [8–10] is the most popular entanglement measure for mixed states. For systems described by Conformal Field Theory, its behaviour has been fully characterised, both at zero temperature [11], and at finite temperature [12]. Similar to the mutual information, for any temperature the negativity exhibits the area-law scaling, which has been checked in several systems [13–17].

An important question, which is key in this paper, is how quantum and classical fluctuations are intertwined at a finite temperature critical point. An important remark is that typical *local* one dimensional models do not exhibit finite-temperature or mid-spectrum criticality, with the notable exception of models that exhibit the many-body localisation transition [18]. It has been argued that entanglement-related quantities can be used to detect this transition [4, 19–21], although no conclusion has been reached, due to the severe finite-size effects. On the other hand, although standard finite-temperature phase transitions are possible in higher dimensions, the interplay between classical and quantum fluctuations at finite-temperature criticality has been scarcely studied, despite growing interest [22–24]. Much effort has focused on the behaviour of the mutual information. For instance, it has been suggested [25–30] that the mutual information exhibits a crossing for different sizes at a finite-temperature critical point, similar to more traditional tools in critical phenomena, such as the Binder cumulant [31].

Importantly, there is growing interest to understand the behaviour of the logarithmic negativity at finite-temperature criticality. An important question is whether the logarithmic negativity exhibits signatures of criticality. Since finite-temperature phase
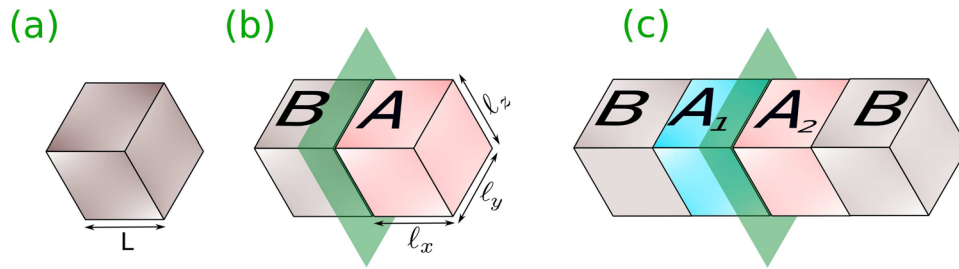
**Figure 1.** Geometry used in this work. The QSM lives on a $3D$ cubic lattice of linear size $L$ (see (a)). Periodic boundary conditions are used in all directions. In (b) the total system is divided into two parts as $A \cup B$, and $B$ is traced over. Here $\ell_x \times \ell_y \times \ell_z$ is the volume of $A$. In (c) subsystem $A$ is further divided as $A = A_1 \cup A_2$. Here we consider the entanglement between the two adjacent cubic blocks $A_1$ and $A_2$. We consider both the case of finite $B$, as well as the limit of $B$ infinite.

transitions are driven by classical fluctuations, and the negativity is only sensitive to true quantum correlations, one should expect the negativity to be smooth across a finite-temperature critical point. Surprisingly, it has been observed that the negativity can exhibit 'weak' singularities, such as cusp-like features, at the critical point [16, 17, 32]. On the other hand, similar singularities have been also observed in the area-law prefactor of the Rényi entropies at quantum phase transitions [33, 34].

In this paper we investigate the behaviour of several entanglement-related observables at finite-temperature criticality. Specifically, we consider the Rényi entropies (and the von Neumann entropy), the mutual information, and the logarithmic negativity. We also discuss the so-called single-particle entanglement spectrum and the negativity spectrum. To be specific, here we focus on the paradigmatic quantum spherical model (QSM) in three dimensions. Spherical models have a venerable history, as they served as test ground for the theory of critical phenomena and the theory of finite-size scaling [35, 36]. The phase diagram of the model (see figure 2) is spanned by the temperature $T$ and the so-called quantum coupling $g$. The latter measures the strength of the quantum fluctuations. In three dimensions, the model exhibits a line of finite-temperature second-order phase transitions between a paramagnetic phase and a ferromagnetically ordered phase. The universality class of the transition has been characterised analytically, since the model is exactly solvable, and it is that of the $N$-vector model [31] in the limit $N \rightarrow \infty$ limit [37]. Surprisingly, the entanglement properties of spherical models have not been explored much.

First, we verify that the entanglement entropy and the Rényi entropies exhibit the expected volume-law in the whole phase diagram. In the thermodynamic limit, the prefactor of the volume-law and its first derivative with respect to the model parameters and the temperature are continuous across the transition. We refer to this behaviour as *regular*. Conversely, we refer to non-analytic behaviour as *singular*. This means that, although the entanglement entropies contain singular contributions, these vanish at the transition as $|g - g_c|^\kappa$ (or as $|T - T_c|^\kappa$) with $\kappa > 1$, and $T_c$ and $g_c$ marking the critical point. The mutual information between two regions exhibits the expected area-law behaviour for any value of $g$ and $T$. Moreover, although the prefactor of the area law contains both regular and singular contributions at criticality, again, we

observe regular behaviour across the transition, suggesting that the singular terms vanish. Interestingly, for finite-size systems we observe that the mutual information does not exhibit a universal crossing at the transition. This reflects that the singular terms, which contain universal information, are vanishing at the critical point, and the mutual information is dominated by non-universal contributions. We find a similar behaviour for the logarithmic negativity. The negativity exhibits the expected area-law in the whole phase diagram. The area-law prefactor has a maximum at the phase transition. In the paramagnetic phase the negativity vanishes as $1/g$ in the limit $g \to \infty$. In the ordered phase it depends mildly on the system parameters for low enough temperature and large enough values of $g$. For any fixed value of $g$, the negativity exhibits a 'sudden death' upon increasing the temperature. Specifically, there is a negativity 'death line', above which the negativity is exactly zero. Interestingly, in the limit $g \to 0$, i.e. when the model becomes classical, the death line exhibits the behaviour $\propto g^{1/2}$. Importantly, at finite temperature the prefactor of the area-law is regular across the para-ferro transition, whereas it develops a cusp-like feature upon lowering the temperature.

Finally, we discuss the single-particle entanglement spectrum [4] and the negativity spectrum [38]. For two nearest-neighbour sites in an infinite system, the spectrum contains only two levels. One of the levels is regular across the transition, whereas the other exhibits a cusp singularity. This is different for the negativity between two extended subsystems. Specifically, we observe that the majority of the single-particle entanglement spectrum levels show regular behaviour at the transition. Only the larger levels exhibit a cusp-like behaviour. Interestingly, the corresponding eigenvectors show a flat-in-space structure, suggesting that the singular levels originate from the zero mode, which is associated with the symmetry breaking. As it is well known, this zero mode leads to sub-leading logarithmic terms [39, 40] in the entropies. This also means that, although the prefactor of the volume law behaviour of the entropies is regular across the transition, the sub-leading corrections exhibit signatures of the criticality. We observe a similar structure for the negativity spectrum. However, since the larger negativity spectrum levels do not contribute to the logarithmic negativity, this suggests that the sub-leading singular terms are suppressed.

The manuscript is organised as follows. In section 2 we introduce the entanglement-related quantities that we consider in the paper. In section 3 we review the QSM. Specifically, in section 3.1 we provide the results for the two-point correlation functions, discussing their behaviour in the paramagnetic phase, and in the ordered phase (in section 3.2 and section 3.3, respectively). In section 4 we address the critical behaviour of the model. Criticality is encoded in the so-called spherical parameter that we discuss in section 4.1. In section 4.2 we focus on the correlators near the para-ferro transition. In order to compare entanglement-related quantities with standard thermodynamic ones, in sections 4.3 and 4.4 we discuss the singular behaviour of the free energy, and of the universal ratio $R_\xi$. In section 5 we focus on the interplay between entanglement and finite-temperature criticality. In sections 5.2 and 5.3 we study the entanglement entropy, and the mutual information. In section 6 we present our results for the logarithmic negativity. In section 6.1 we focus on the negativity between two sites embedded in an infinite system, whereas in section 6.2 we discuss the negativity between two extended regions. In section 7 we investigate the single-particle entanglement spectrum and the negativity spectrum. Finally, we conclude in section 8.
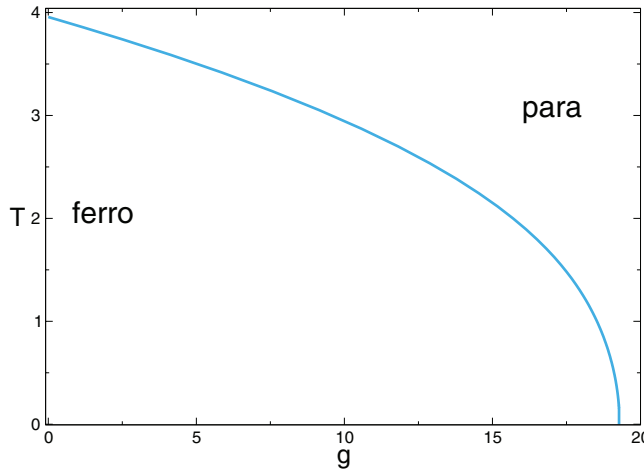
**Figure 2.** Phase diagram of the 3D QSM. $T$ is the temperature and $g$ measures the strength of quantum fluctuations (quantum coupling). At low temperature and small $g$ the model is in a ferromagnetic ordered phase. This is destroyed upon increasing $T$ and $g$, and the model becomes paramagnetic. The continuous line marks a second-order phase transition. At $T = 0$ the system undergoes a quantum phase transition. At any $T \neq 0$ the critical behaviour of the system is in the same universality class as that of the classical spherical model at $g = 0$.

## 2. Entanglement entropies, mutual information & logarithmic negativity: definitions

In this section we introduce the definitions of the entanglement and Rényi entropies, the mutual information, and the so-called logarithmic negativity. Here, we always consider a system on a 3D cubic lattice of linear size $L$ (see figure 1(a)), prepared in a thermal state at temperature $T \equiv 1/\beta$.

In order to define the entanglement entropy (von Neumann entropy) and the Rényi entropies, we consider a bipartition of the system into two parts $A$ and $B$ (see figure 1(b)). From the reduced density matrix for $A$, $\rho_A \equiv \mathrm{Tr}_B \rho$, with $\rho$ being the density matrix of the full system, we define the Rényi entropies $S_{n,A}$ as [1–4]

$$S_{n,A} = \frac{1}{1-n} \mathrm{Tr}\rho_A^n, \quad \text{with } n \in \mathbb{R}. \tag{2}$$

In the limit $n \to 1$ one obtains the von Neumann entropy as

$$S_{\mathrm{vN}} = -\mathrm{Tr}\rho_A \ln \rho_A. \tag{3}$$

Both, the von Neumann and the Rényi entropies, are good entanglement measures for pure systems, for instance bipartite systems at zero temperature. This is not the case anymore if $A \cup \bar{A}$, with $\bar{A}$ the complement of $A$, is in a mixed state, for instance a thermal one. In a thermal state, $S_{n,A}$ exhibits a volume-law behaviour $S_{n,A} \propto L^d$. For $S_{\mathrm{vN}}$, the prefactor of the volume-law is the same as that of the *thermal* entropy, i.e. the von Neumann entanglement entropy becomes the thermodynamic entropy at finite temperature [41–43].

The mutual information between two subsystems is defined for the typical geometry depicted in figure 1(c). The subsystem $A$ is divided into two complementary parts viz

$A_1 \cup A_2 = A$, with $\bar{A}$ in general not empty. The mutual information $I_{n,A_1:A_2}$ is defined as

$$I_{n,A_1:A_2} = S_{n,A_1} + S_{n,A_2} - S_{n,A_1 \cup A_2}. \tag{4}$$

Here $S_{n,X}$ is the Rényi entropy of subsystem $X$. It is important to note that the mutual information is only a measure of the total correlation shared between the two subsystems, and not of the shared entanglement. This is because $I_{n,A_1:A_2}$ is sensitive to both, quantum and classical correlations, which is reflected in the fact that $A$ is in a mixed state. Importantly, this is also the case at $T = 0$ if $A_1 \cup A_2$ is not the full system, i.e. if $A_1$ and $A_2$ are not complementary intervals. In this case the classical correlation originates from the trace over the environment, i.e. $\bar{A}$ in (4). It can be shown, however, that the mutual information provides a bound to the mutual entanglement [9].

Both the entanglement entropy and the mutual information have been studied intensely as possible witnesses of critical behaviour in several systems (see [4] for a review), both at finite-temperature phase transitions [25, 26, 28, 29, 44–46], or at $T = 0$ phase transitions [27, 30, 33, 34, 47]. Specifically, in [25] (see also [26]) it has been suggested that the mutual information densities $I_{n,A_1:A_2}/L^{d-1}$ exhibit a crossing at $T = T_c$ and $T = nT_c$. On the other hand, at zero temperature, it has been shown that the area-law coefficient of the entanglement entropy displays a cusp-like singularity across a second order phase transition (see for instance [33]).

Here we also consider the so-called logarithmic negativity [8–10, 48–50]. Unlike the mutual information, the negativity is a good entanglement measure for mixed states. The negativity allows, for instance, to quantify the entanglement in a bipartite system at finite temperature (see figure 1(b)), or the entanglement between two non-complementary subsystems (as in figure 1(c)) at zero temperature. The negativity is defined from the so-called partial transpose. Given the partition of $A$ as $A = A_1 \cup A_2$ (see figure 1(c)), the matrix elements of the partial transpose $\rho_A^{T_2}$ with respect to the degrees of freedom of $A_2$ are defined as

$$\langle \varphi_1 \varphi_2 | \rho_A^{T_2} | \varphi_1' \varphi_2' \rangle = \langle \varphi_1 \varphi_2' | \rho_A | \varphi_1' \varphi_2 \rangle. \tag{5}$$

Here $\{\varphi_1\}$ and $\{\varphi_2\}$ are two orthonormal bases for $A_1$ and $A_2$, respectively. Interestingly, the eigenvalues $\zeta_i$ of $\rho_A^{T_2}$ can be both positive and negative. This is in contrast with the eigenvalues of $\rho_A$, which can be only positive. The logarithmic negativity $\mathcal{E}_{A_1:A_2}$ is defined as

$$\mathcal{E}_{A_1:A_2} = \ln \mathrm{Tr} |\rho_A^{T_2}|. \tag{6}$$

Recently, the negativity has become a useful tool to characterise universal aspects of quantum many-body systems [11, 12, 32, 38, 51–78], also because it can be computed with matrix product states (MPS) methods [51, 55, 57]. The negativity (6) can be obtained for free-bosonic models in arbitrary dimension by correlation matrix techniques [13, 14, 79]. This is not possible for free-fermion models [80–87]. An alternative entanglement measure, which is effectively calculable using free-fermion techniques, has been introduced [15, 85, 86, 88–90], and it is also an upper bound for the negativity [87]. Very recently, much attention has been focused to study the behaviour of the negativity at a finite-temperature phase transition. It has been suggested in [16] and [17]

that in some cases the logarithmic negativity exhibits a cusp-like singularity, i.e. it is sensitive to the classical criticality, although it is a measure of quantum entanglement.

## 3. Quantum spherical model

The QSM [91, 92] is defined on a $3D$ cubic lattice of volume $V = L^3$, with $L$ the lattice linear size (see figure 1). The Hamiltonian reads

$$H = \frac{g}{2} \sum_n p_n^2 - \sum_{\langle n,m \rangle} s_n s_m + (\mu - 3) \sum_n s_n^2. \tag{7}$$

In equation (7), $n = (n_x, n_y, n_z)$ denotes a generic lattice site, and $\langle n, m \rangle$ a lattice bond joining two nearest-neighbour sites. Here $s_n$ and $p_n$ are canonically conjugated variables satisfying the commutation relations

$$[p_n, p_m] = [s_n, s_m] = 0, \quad [s_n, p_m] = i\delta_{nm}. \tag{8}$$

In equation (7), $\mu$ and $g$ are real parameters. The first term in equation (7) is a kinetic term, which makes the model quantum. The parameter $g$ is the quantum coupling. For $g = 0$ the model becomes classical and it reduces to the famous spherical model [93, 94]. The spherical parameter $\mu$ is fixed by imposing the spherical constraint as

$$\sum_n \langle s_n^2 \rangle = V, \tag{9}$$

where $\langle \cdot \rangle$ denotes the average over the thermal ensemble. The additive shift by 3 in the definition of the spherical parameter in (7) is solely for later convenience and routinely not performed in literature. Critical properties (for instance, critical exponents) of the QSM are determined by the behaviour of $\mu$.

In order to diagonalise $H$, one exploits the translational invariance of the system by defining the Fourier transformed operators $\pi_k$ and $q_k$ as

$$p_n = \frac{1}{\sqrt{V}} \sum_k e^{-ink} \pi_k, \qquad s_n = \frac{1}{\sqrt{V}} \sum_k e^{ink} q_k. \tag{10}$$

Here the sum over $k \equiv (k_x, k_y, k_z)$ runs in the first Brillouin zone $k_i \equiv \pi/L j$, with $j \in [-L, L]$ integer. In terms of $q_k, \pi_k$ the Fourier representation of the Hamiltonian becomes

$$H = \sum_k \frac{g}{2} \pi_k \pi_{-k} + \Lambda_k^2 q_k q_{-k}. \tag{11}$$

The single-particle dispersion $\Lambda_k$ reads

$$\Lambda_k = \sqrt{\mu + \omega_k} \quad \text{with} \quad \omega_k = \sum_{j=x,y,z} (1 - \cos k_j). \tag{12}$$

To completely diagonalise (11) we introduce ladder operators $b_k$ and $b_k^\dagger$ as

$$q_k = \alpha_k \frac{b_k + b_{-k}^\dagger}{\sqrt{2}}, \qquad \pi_k = \frac{\mathrm{i}}{\alpha_k} \frac{b_k^\dagger - b_{-k}}{\sqrt{2}}, \tag{13}$$

with $\alpha_k^2 = \sqrt{g/2}\,\Lambda_k^{-1}$. The operators $b_k$ obey standard bosonic commutation relations. By using (13), the Hamiltonian (11) becomes diagonal, and it is given as

$$H = \sum_k E_k(b_k^\dagger b_k + 1/2), \quad \text{with} \qquad E_k = \sqrt{2g}\,\Lambda_k. \tag{14}$$

In an equilibrium thermal ensemble, the modes $k$ are occupied according to the Bose–Einstein distribution

$$\langle b_k b_{k'}\rangle = \langle b_k^\dagger b_{k'}^\dagger\rangle = 0 \quad, \quad \langle b_k^\dagger b_{k'}\rangle = \frac{\delta_{kk'}}{1 - \mathrm{e}^{\beta E_k}}, \tag{15}$$

where $\beta = 1/T$ is the inverse temperature.

The QSM has been studied extensively in any dimension. In three dimensions, the model exhibits a finite-temperature second-order phase transition between a high-temperature paramagnetic phase and a low-temperature ferromagnetic (ordered) phase. The universality class of the transition is the same as that of the classical spherical model, and it has been fully characterised [35] (see also [36]). The universality class is the same as that of the $N$-vector model at $N \to \infty$. At $T = 0$ the model undergoes a second-order quantum phase transition at a critical $g_c$. The universality class of the transition is the same as that of the classical spherical model in $3 + 1$ dimensions [95], as expected from renormalisation group arguments. Critical properties of the model are determined by the behaviour of $\mu$. For any temperature, $\mu \geqslant 0$ for $g > g_c$. On the other hand, one has $\mu = 0$ for $g < g_c$, i.e. in the ordered phase, which signals non-analytic behaviour. The phase diagram of the model is reported in figure 2. The continuous line is the critical line marking the second-order phase transition between the ferromagnetic phase at small $g$ and low temperature, and the standard paramagnetic phase.

### 3.1. Two-point correlation functions

The key ingredients to study entanglement-related quantities in the QSM are the two-point correlators of the operators $s_n$ and $p_n$ (see (7)) at equilibrium. They can be readily obtained by first expressing $s_n, p_n$ in terms of $b_k, b_k^\dagger$ that diagonalise the model, and using (15). One obtains [96]

$$\langle s_n s_m\rangle = \frac{1}{2V} \sum_k \mathrm{e}^{\mathrm{i}(n-m)\cdot k} \alpha_k^2 \coth(\beta E_k/2) \tag{16}$$

$$\langle p_n p_m\rangle = \frac{1}{2V} \sum_k \mathrm{e}^{\mathrm{i}(n-m)\cdot k} \alpha_k^{-2} \coth(\beta E_k/2) \tag{17}$$

$$\langle s_n p_m\rangle = \frac{\mathrm{i}}{2}\delta_{nm}. \tag{18}$$

Here we defined $k \equiv (k_x, k_y, k_z)$. Note that in the thermodynamic limit, at the critical point one has that $\mu = 0$, and the contribution of the zero mode with $k_x = k_y = k_z = 0$

diverges. This is not the case at finite $L$, because for a finite system $\mu$ is nonzero for any $g$ and $\beta$ (see section 4.1). Clearly, one can rewrite (16) as

$$\langle s_n s_m \rangle = \frac{1}{\sqrt{V}} \mathcal{F}_d^{-1}\left(\alpha_k^2 \coth(\beta E_k/2)\right)(n-m),\tag{19}$$

where $\mathcal{F}_d^{-1}(x)$ denotes the inverse Fourier transform of $x$ in $d$ dimensions. Equation (19) is more suitable than (16) for numerical computations because there are very efficient methods for evaluating the Fourier transform.

From (16), the constraint (9) for the spherical parameter $\mu$ reads

$$\frac{2}{g} = \frac{1}{V} \sum_k \frac{\coth(\beta E_k/2)}{E_k}.\tag{20}$$

The free energy $F$ of the QSM reads as

$$F = TL^3 \ln 2 + T \sum_{k_x,k_y,k_z=0}^{L-1} \ln \sinh\left[\frac{1}{T}\sqrt{\frac{g}{2}}\left(\mu + 3 - \sum_{j=x,y,z} \cos\left(\frac{2\pi k_j}{L}\right)\right)^{\frac{1}{2}}\right].\tag{21}$$

The expressions for (16)–(18) and (21) in the thermodynamic limit $L \to \infty$ are obtained, as usual, by replacing

$$\frac{2\pi k_j}{L} \to k_j',\tag{22}$$

$$\frac{1}{L^3} \sum_{k_x,k_y,k_z} \to \prod_{j=x,y,z} \int_{-\pi}^{\pi} \frac{\mathrm{d}k_j'}{2\pi}.\tag{23}$$

In the following sections we discuss the behaviour of the correlators (16)–(18) in the paramagnetic phase at large $g$, and in the low-temperature ordered phase.

### 3.2. Paramagnetic phase: large $g$ expansion

Here we discuss the large $g$ expansion of the correlators in the paramagnetic phase, in the thermodynamic limit. To this purpose, one has to first determine the behaviour of the spherical parameter $\mu$, which is obtained by solving equation (30), in the large $g$ limit. We numerically verified that $\mu \to \infty$ for $g \to \infty$. Moreover, by taking the limit $g \to \infty$ in (30), and using the definition of $E_k$ (see (11)), one obtains that the leading behaviour of $\mu$ is $\mu + 3 = g/8 + o(g)$. To derive the higher order corrections, it is natural to conjecture that $\mu$ has the following expansion

$$\mu + 3 = \frac{g}{8} + \frac{C_1}{g} + \frac{C_3}{g^3} + \mathcal{O}(g^{-5}).\tag{24}$$

The coefficients $C_1$ and $C_3$ can be determined by substituting the ansatz (24) in (30), expanding for $g \to \infty$, and equating the terms with the same power of $g$. After doing that, and after neglecting exponentially suppressed terms, one obtains

$$C_1 = 9, \quad C_3 = 441.\tag{25}$$

Higher order terms can be obtained in a similar way. The behaviour of the correlation functions (16) and (17) at large $g$ is easily obtained after substituting (24), and expanding at large $g$. This yields

$$\langle s_n s_m \rangle = \frac{\sqrt{g}}{2\sqrt{2}} \int \frac{\mathrm{d}k}{(2\pi)^3} \frac{\mathrm{e}^{\mathrm{i}(n-m)k}}{\sqrt{\mu + \omega_k}} = \delta_{nm} + \frac{2}{g}\delta_{|n-m|,1} + o(1/g) \tag{26}$$

$$\langle p_n p_m \rangle = \frac{1}{\sqrt{2g}} \int \frac{\mathrm{d}k}{(2\pi)^3} \mathrm{e}^{\mathrm{i}(n-m)k} \sqrt{\mu + \omega_k} = \frac{1}{4}\delta_{nm} - \frac{1}{2g}\delta_{|n-m|,1} + o(1/g). \tag{27}$$

Here $\delta_{|n-m|,1} = \prod_{j=x,y,z} \delta_{|n_j-m_j|,1}$. Clearly, longer-range correlations are suppressed with higher powers of $1/g$, as expected because the model is paramagnetic, and correlation functions decay exponentially at large distances.

### 3.3. Ferromagnetic phase: low-temperature expansion

We now discuss the behaviour of the model at low temperature in the thermodynamic limit. In the ordered phase one has $\mu = 0$. In the limit $\beta \to \infty$ one can replace $\coth(\beta x) \to 1$ in (16) and (17). The next-to-the-leading behaviour at large $\beta$ is obtained by using the standard saddle point method. One obtains the expansions for the correlators (16) and (17) as

$$\langle s_n s_m \rangle = \frac{\sqrt{g}}{2\sqrt{2}} \int \frac{\mathrm{d}k}{(2\pi)^3} \frac{\mathrm{e}^{\mathrm{i}k(n-m)}}{\sqrt{\omega_k}} + \frac{1}{12\beta^2\sqrt{g}} + o(1/\beta^2) \tag{28}$$

$$\langle p_n p_m \rangle = \frac{1}{\sqrt{2g}} \int \frac{\mathrm{d}k}{(2\pi)^3} \mathrm{e}^{\mathrm{i}k(n-m)} \sqrt{\omega_k} + \frac{\pi^2}{30g^{5/2}\beta^4} + o(1/\beta^4). \tag{29}$$

As it is clear from (28) and (29), the leading behaviour of $\langle s_n s_m \rangle$ is determined by the integral of $1/\sqrt{\omega_k}$. The first sub-leading correction to $\langle s_n s_m \rangle$ is $\mathcal{O}(1/(\beta^2 g^{1/2}))$, whereas for $\langle p_n p_m \rangle$ it is $\mathcal{O}(1/(\beta^4 g^{5/2}))$. Note that the sub-leading corrections do not depend on $n, m$. A similar behaviour occurs at criticality (see section 4), and it has important consequences for the singularity structure of entanglement-related quantities.

## 4. Critical behaviour of the QSM

Here we are interested in the critical behaviour of the QSM at finite temperature. The main goal of this section is to derive the behaviour of the two-point correlators in the vicinity of the para-ferro transition (see figure 2). To do that we first derive the expansion for the spherical parameter near the critical point (see section 4.1). In section 4.2 we present our results for the correlators. In order to compare the behaviour of entanglement-related quantities at the finite-temperature phase transition with that of standard quantities, in sections 4.3 and 4.4 we discuss the scaling of the free energy and the universal ratio $R_\xi$ at criticality.

### 4.1. Spherical parameter

The critical behaviour of both the classical and the QSM is determined by the spherical parameter $\mu$ (see (9)). It is somewhat easier to work in the thermodynamic limit, although the finite-size behaviour of $\mu$ can be derived using standard techniques [97]. In the thermodynamic limit, equation (9) becomes (see section 3.1)

$$\frac{2}{g} = \int \frac{\mathrm{d}k}{(2\pi)^3} \frac{\coth(\beta E_k/2)}{E_k}. \tag{30}$$

To proceed let us first rewrite (30) as

$$1 = \frac{\sqrt{g}}{2\sqrt{2}} \int \frac{\mathrm{d}k}{(2\pi)^3} \frac{\coth(\beta\sqrt{g/2}\sqrt{\mu+\omega_k})}{\sqrt{\mu+\omega_k}}, \tag{31}$$

with $\omega_k$ as defined in (12). Near criticality, on the paramagnetic side, one has $\mu \to 0$, whereas $\mu = 0$ everywhere in the ordered phase. This reflects the presence of singular terms in the expansion of $\mu$ near the transition. To derive these terms at the leading order in $g - g_c$, it is convenient to expand (31) for small $\mu + \omega_k$. The reason is that the singular terms are determined by the singularity at small $k$ of the integrand in (31). One has

$$1 = \frac{\sqrt{g}}{2\sqrt{2}} \int \frac{\mathrm{d}k}{(2\pi)^3} \frac{\coth(\beta\sqrt{g/2}\sqrt{\mu+\omega_k})}{\sqrt{\mu+\omega_k}} = \int \frac{\mathrm{d}k}{(2\pi)^3} \left[ \frac{1}{2\beta(\mu+\omega_k)} + a_k(\mu,\beta,g) \right]. \tag{32}$$

Here $a(\mu,\beta,g)$ is an analytic function of its arguments. The first few terms of its series expansion read

$$a_k(\mu,\beta,g) = \frac{g\beta}{12} - \frac{g^2\beta^3}{360}(\mu+\omega_k) + \frac{g^3\beta^5}{7560}(\mu+\omega_k)^2 + \dots, \tag{33}$$

where the dots denote higher order terms. Importantly, at the leading order in $\mu$ one has $a_k = \mathcal{O}(\mu)$. The first term in the square brackets in (32) encodes the critical behaviour of the model. The integral is the celebrated Watson integral [98]. The same integral appears in the classical spherical model, reflecting that for nonzero $T$ the universality class of the transition is the same as that of the classical model. It is interesting to observe that the integral can be expressed explicitly in terms of hypergeometric functions [99]. For instance for $\mu = 0$ one has

$$\int \frac{\mathrm{d}k}{(2\pi)^3} \frac{1}{\omega_k} = \frac{\sqrt{2}}{32\sqrt{3}\pi^3} \Gamma(1/24)\Gamma(5/24)\Gamma(7/24)\Gamma(11/24). \tag{34}$$

To proceed, one subtracts from (33) the expansion of the equation for the spherical parameter (30) at $g = g_c$. One obtains

$$\int \frac{\mathrm{d}k}{(2\pi)^3} \left[ -\frac{\mu}{2\beta\omega_k(\mu+\omega_k)} + a_k(\mu,\beta,g) - a_k(0,\beta,g_c) \right] = 0. \tag{35}$$

The leading behaviour in $\mu$ of the integral in (35) is obtained by expanding $\omega_k$ for $k \to 0$. One now has

$$\int \frac{\mathrm{d}k}{(2\pi)^3} \frac{\mu}{2\beta\omega_k(\mu + \omega_k)} = \int \frac{\mathrm{d}k}{(2\pi)^3} \frac{\mu}{\beta|k^2|(\mu + |k|^2/2)} + \mathcal{O}(\mu)$$

$$= \frac{1}{\beta} \int_{-\pi/\sqrt{\mu}}^{\pi/\sqrt{\mu}} \frac{\mathrm{d}y}{(2\pi)^3} \frac{\sqrt{\mu}}{|y|^2(1 + |y|^2/2)} = \frac{\sqrt{2\mu}}{4\pi\beta} + \mathcal{O}(\mu). \quad (36)$$

In the last steps we changed variables to spherical coordinates with $y \equiv |k|$, performing the integration on a sphere of radius $\pi/\sqrt{\mu}$, instead of the cube $[-\pi/\sqrt{\mu}, \pi/\sqrt{\mu}]$. This introduces a $\mathcal{O}(\mu)$ term. Since the leading order is $\mathcal{O}(\sqrt{\mu})$, this is negligible in the limit $g \to g_c$. Note that the term $\sqrt{\mu}$ is singular at $g_c$.

Since we are interested in the leading $\mathcal{O}(\sqrt{\mu})$ behaviour, and $a_k(\mu, \beta, g) = \mathcal{O}(\mu)$ we can set $\mu = 0$ in $a_k$. We also observe that

$$a_k(0, \beta, g) - a_k(0, \beta, g_c) = \frac{\sqrt{g}}{2\sqrt{2}} \frac{\coth(\beta\sqrt{g\omega_k}/2)}{\sqrt{\omega_k}} - \frac{\sqrt{g_c}}{2\sqrt{2}} \frac{\coth(\beta\sqrt{g_c\omega_k}/2)}{\sqrt{\omega_k}}. \quad (37)$$

At the leading order in $g - g_c$, from (33), (35) and (37) we obtain

$$\mu = \frac{\beta^2}{128\pi^4} \left[ \int \mathrm{d}k \left( \frac{\beta}{2} + \frac{\coth(\beta\sqrt{g_c\omega_k}/2)}{\sqrt{2g_c\omega_k}} - \frac{\beta}{2}\coth^2(\beta\sqrt{g_c\omega_k}/2) \right) \right]^2 (g - g_c)^2 + o((g - g_c)^2). \quad (38)$$

It is also convenient to expand the integrands in (38) at small $k$, to obtain

$$\mu = \frac{\pi^2\beta^4}{7200}(g - g_c)^2(20 + \beta^2 g_c(\beta^2 g_c - 4))^2 + \ldots \quad (39)$$

In a similar way, one can derive the expression for $\mu$ if the transition is approached at fixed $g$ by varying the temperature. One obtains

$$\mu = 8\pi^2 \left[ 1 - \int \frac{\mathrm{d}k}{(2\pi)^3} \left( \frac{\beta_c g}{4} + \frac{\sqrt{g}\coth(\beta_c\sqrt{g\omega_k}/2)}{2\sqrt{2\omega_k}} - \frac{\beta_c g}{4}\coth^2(\beta_c\sqrt{g\omega_k}/2) \right) \right]^2 (\beta - \beta_c)^2 + o((\beta - \beta_c)^2). \quad (40)$$

Again, after expanding for small $k$, one has

$$\mu = \frac{2\pi^2}{2025}(\beta - \beta_c)^2(90 + g\beta_c(-15 + \beta_c^2 g - 6\beta_c^4 g^2))^2 + \ldots \quad (41)$$

Note that the expected behaviours [95] $\mu \propto (g - g_c)^2$ and $\mu \propto (\beta - \beta_c)^2$ hold. Finally, a similar calculation [97] should allow, in principle, to extract the finite-size behaviour of $\mu$.

The correctness of (38) and (40) is verified in figure 3. The symbols in the figure are the values of $\mu$ obtained by solving (30). The dashed-dotted lines are the analytical results (38) and (40). Note that (38) and (40) hold only in the vicinity of the transition (in the figure $g - g_c \approx 10^{-2}$ and $\beta - \beta_c \approx 10^{-3}$).

It is also useful to check how the thermodynamic limit is approached. In figure 4 we report numerical results for $\mu$ for finite-size systems. These are obtained by solving numerically (20). In the figure we plot $3 + \mu$ versus $g$. The data are for fixed temperature $T = 1$, although similar results are obtained for different temperatures. The vertical dotted line denotes the critical coupling $g_c$. The dashed-dotted line is the result for

$\mu$ in the thermodynamic limit, i.e. obtained by solving (30). Clearly, $\mu = 0$ for $g \leqslant g_c$, whereas $\mu \to \infty$ in the limit $g \to \infty$.

The different symbols are the finite-size results for $\mu$. One obtains a nonzero value for $\mu$ for any $g$. As it is clear from the figure, both in the paramagnetic and in the ferromagnetic regions the data quickly converge to the thermodynamic limit (dashed-dotted line). Around the critical point, large finite-size effects are present. The perturbative result for $\mu$ (see (24)) is reported in figure 4 as dashed-dotted line. Although the agreement is not perfect for the values of $g$ reported in the figure, we checked that the result (24) is recovered upon increasing $g$.

### 4.2. Two-point correlators

By using the expansion for $\mu$ near the critical line that we derived in the previous section, it is now straightforward to obtain the two-point correlation functions. Again, the idea is to expand $\omega_k$ around $k = 0$ in (16) and (17) in the thermodynamic limit. For the case in which the transition is approached at fixed $T$, one obtains

$$
\begin{aligned}
\langle s_n s_m \rangle = {} & \frac{\sqrt{g_c}}{2\sqrt{2}} \int \frac{\mathrm{d}k}{(2\pi)^3} \frac{\coth(\beta\sqrt{g_c \omega_k/2})}{\omega_k} \mathrm{e}^{ik(n-m)} \\
& + (g - g_c) \int \frac{\mathrm{d}k}{(2\pi)^3} \Big( \frac{\beta}{8} + \frac{\coth(\beta\sqrt{g_c \omega_k/2})}{4\sqrt{2 g_c \omega_k}} \\
& - \frac{\beta}{8} \coth^2(\beta\sqrt{g_c \omega_k/2}) \Big) \mathrm{e}^{ik(n-m)} - \frac{\sqrt{2\mu}}{4\pi\beta} + \mathcal{O}((g - g_c)^2).
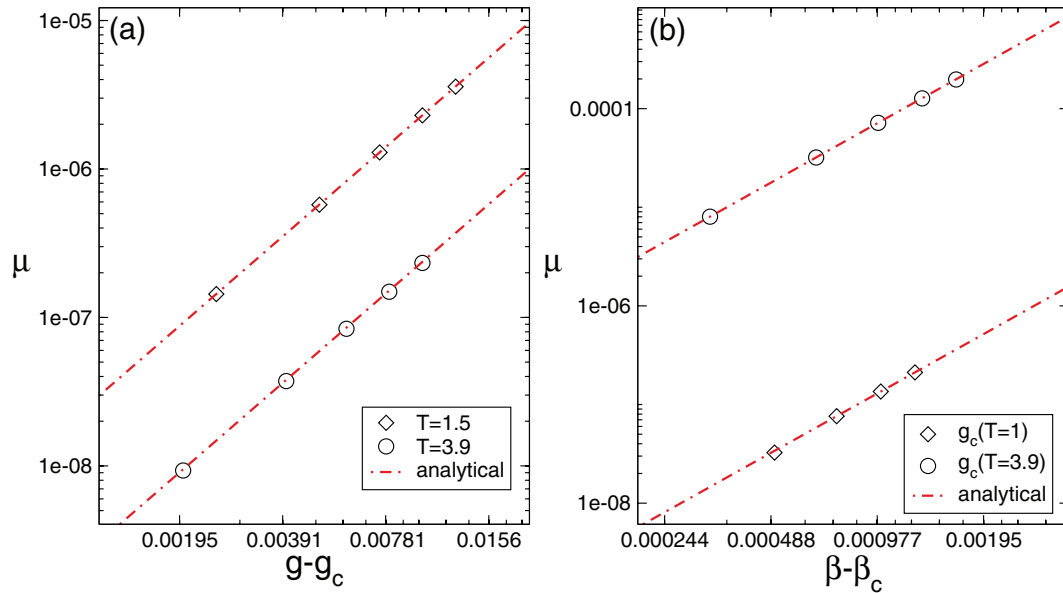\end{aligned}
\tag{42}
$$

If the critical point is approached at fixed $g$, one has

$$
\begin{aligned}
\langle s_n s_m \rangle = {} & \frac{\sqrt{g}}{2\sqrt{2}} \int \frac{\mathrm{d}k}{(2\pi)^3} \frac{\coth(\beta_c\sqrt{g \omega_k/2})}{\sqrt{\omega_k}} \mathrm{e}^{ik(n-m)} \\
& + \frac{g}{4}(\beta - \beta_c) \int \frac{\mathrm{d}k}{(2\pi)^3} \Big( 1 - \coth^2(\beta_c\sqrt{g \omega_k/2}) \Big) \mathrm{e}^{ik(n-m)} - \frac{\sqrt{2\mu}}{4\pi\beta_c} + \mathcal{O}((\beta - \beta_c)^2).
\end{aligned}
\tag{43}
$$

For the correlators $\langle p_n p_m \rangle$, a similar calculation yields

$$
\begin{aligned}
\langle p_n p_m \rangle = {} & \frac{1}{\sqrt{2 g_c}} \int \frac{\mathrm{d}k}{(2\pi)^3} \coth(\beta\sqrt{g_c \omega_k/2}) \sqrt{\omega_k} \mathrm{e}^{ik(n-m)} \\
& + \frac{g - g_c}{g_c} \int \frac{\mathrm{d}k}{(2\pi)^3} \omega_k \\
& \Big( \frac{\beta}{4} - \frac{\coth(\beta\sqrt{g_c \omega_k/2})}{2\sqrt{2\omega_k g_c}} - \frac{\beta}{4}\coth^2(\beta\sqrt{g_c \omega_k/2}) \Big) \mathrm{e}^{ik(n-m)} + \mathcal{O}((g - g_c)^2).
\end{aligned}
\tag{44}
$$

**Figure 3.** Spherical parameter $\mu$ near the para-ferro transition on the paramagnetic side. In (a) and (b) we approach the transition at fixed temperature and fixed $g$, respectively. The symbols are exact numerical results in the thermodynamic limit obtained by solving (30). The lines are the analytical results near the critical point (see (38) and (40)).
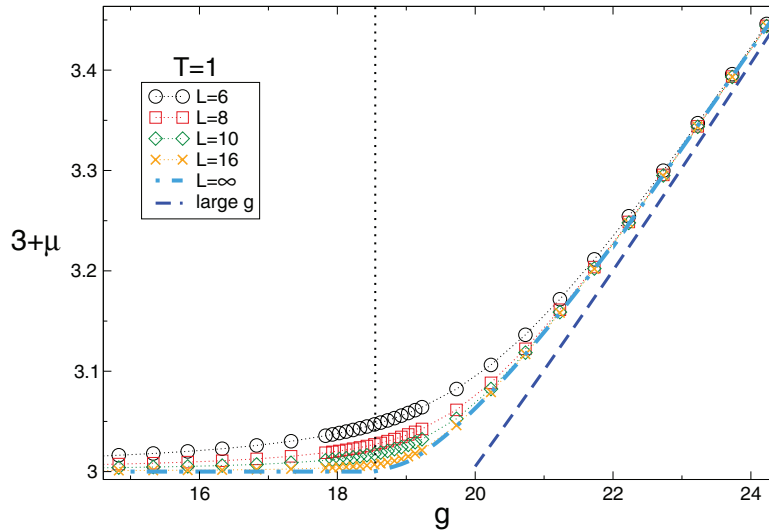


**Figure 4.** Spherical parameter $\mu$ in the QSM at finite temperature: $3 + \mu$ plotted versus $g$ at fixed temperature $T = 1$. The symbols are the finite-size results for several lattice sizes $L$. Results are obtained by solving numerically the equation for the spherical constraint (20). The dashed-dotted line is the result in the thermodynamic limit. The dashed line is the analytical result for large $g$. Note that in the thermodynamic limit $\mu = 0$ below the critical point at $g_c \approx 18.52$ (vertical dotted line). Near the critical point it is $\mu \propto (g - g_c)^2$.

If one approaches the transition along the temperature direction, one obtains

$$
\begin{aligned}
\langle p_n p_m \rangle = & \frac{1}{\sqrt{2g}} \int \frac{\mathrm{d}k}{(2\pi)^3} \coth(\beta_c \sqrt{g\omega_k/2}) \sqrt{\omega_k} \mathrm{e}^{\mathrm{i}k(n-m)} \\
& + \frac{1}{2} \int \frac{\mathrm{d}k}{(2\pi)^3} \omega_k (1 - \coth^2(\beta_c \sqrt{g\omega_k/2})) \mathrm{e}^{\mathrm{i}k(n-m)} (\beta - \beta_c) + \mathcal{O}((\beta - \beta_c)^2).
\end{aligned}
\tag{45}
$$

Clearly, in all cases (see (42)–(45)) the correlation functions are finite at the critical point, and exhibit a $\mathcal{O}(g - g_c)$ and $\mathcal{O}(\beta - \beta_c)$ behaviour. Crucially, in both (42) and (43) one has the singular contribution $\propto \sqrt{\mu}$. On the other hand, this is not present in the expansion of $\langle p_n p_m \rangle$. This implies that the correlator $\langle s_n s_m \rangle$ has a cusp-like singularity across the critical point, whereas $\langle p_n p_m \rangle$ is regular. Finally, one should observe that the singular term in (42) and (43) does not depend on the position. This means that the spatial structure of the correlators appears only in sub-leading contributions in $g - g_c$ that we are neglecting.

### 4.3. Scaling of the free energy

It is instructive to investigate the singular contributions to the free energy. A similar qualitative behaviour will be observed for entanglement-related quantities (see sections 5.2, 5.3 and 6). Let us focus on the situation in which $T$ is kept fixed, and let us study the behaviour around the critical point as a function of $g$. At a second order phase transition the free energy *density* contains both analytic and singular terms. In general it can be written as [31]

$$
f \equiv \frac{F}{L^3} = f_{\mathrm{an}}(g) + f_{\mathrm{sing}}(g).
\tag{46}
$$

The term $f_{\mathrm{an}}$ is the smooth part of the free energy, which depends analytically on the system parameters. The second part $f_{\mathrm{sing}}$ contains the singularities and the universal properties of the model. $f_{\mathrm{sing}}$ obeys the scaling form (see [31] for a review)

$$
f_{\mathrm{sing}}(u_1, u_L, \ldots, u_n) = b^{-d} f_{\mathrm{sing}}(b^{y_1} u_1, u_L b, \ldots, b^{y_n} u_n).
\tag{47}
$$

Here $b > 0$ is an arbitrary number, and $u_n$ are the scaling fields, which are analytic functions of the system's parameters. $y_n$ are the scaling dimensions associated with the fields $u_n$. Here we assume that there are only two relevant scaling fields, $u_1$ and $u_L$. $u_1$ is associated with changing the coupling $g$, and $u_L$ with the finite-size scaling. $u_L$ has scaling dimension $y_L = 1$. We define $y_1 = 1/\nu$. In (47), $y_n < 0$ for $n > 1$, i.e. $u_n$ are irrelevant, which give non-analytic scaling corrections to the free energy. Several scaling laws can be derived from (47). For instance, the finite-size scaling form of the free energy is obtained by choosing $b = 1/u_L$. We obtain

$$
f_{\mathrm{sing}} = u_L^d f_{\mathrm{sing}}(u_1/u_L^{y_1}).
\tag{48}
$$

Using that $u_L \approx 1/L$, and that close to the phase transition $u_1 \approx g - g_c$, we find the standard result

$$
f_{\mathrm{sing}} = L^{-d} f_{\mathrm{sing}}((g - g_c) L^{1/\nu}).
\tag{49}
$$

For a second-order phase transition, the free energy density is finite everywhere in the phase diagram. The singular part $f_{\mathrm{sing}}$ vanishes at the critical point. Indeed, for $g = g_c$

one obtains from (49) the contribution $f_{\text{sing}}(0)L^{-3}$, which is vanishing because $f_{\text{sing}}$ is finite. By choosing $u_1 b^{y_1} = 1$ in (47) in the thermodynamic limit one obtains the scaling behaviour

$$f_{\text{sing}} = |g - g_c|^{\mathrm{d}\nu} f_{\text{sing}}(\text{sign}(g - g_c)) \propto |g - g_c|^{2-\alpha}. \tag{50}$$

Note the dependence on the sign of $g - g_c$. In (50) we used the hyperscaling relation $\mathrm{d}\nu = 2 - \alpha$, with $\alpha$ the critical exponent of the specific heat. In the limit $L \to \infty$ one has to recover (50) from (49). This implies that $f_{\text{sing}}((g - g_c)L^{1/\nu}) \approx |(g - g_c)L|^{\mathrm{d}\nu} f_{\text{sing}}(\pm\infty)$ for $L \to \infty$. We should stress that in the derivations above we neglected all the scaling corrections.

It is interesting to derive the singular behaviour of the free energy in the QSM. We work in the thermodynamic limit. The density of free energy of the QSM reads (see (21))

$$f \equiv \lim_{L\to\infty} \frac{F}{L^3} = \frac{1}{\beta} \ln(2) + \frac{1}{\beta} \int \frac{\mathrm{d}k}{(2\pi)^3} \ln \sinh\left[\beta \sqrt{g/2} \sqrt{\mu + \omega_k}\right]. \tag{51}$$

As for the spherical constraint and for the correlators (see sections 4.1 and 4.2), the idea is to expand (51) for small $k$. After expanding (51), one obtains

$$f = \frac{1}{\beta}(\ln(\beta\sqrt{g/2}) + \ln(2)) + \int \frac{\mathrm{d}k}{(2\pi)^3} \left[\frac{1}{2\beta} \ln(\mu + \omega_k) + b_k(\mu, \beta, g)\right], \tag{52}$$

where $b_k$ denotes an analytic function of its arguments. At the leading order it is given as

$$b_k \equiv \frac{\beta g}{12}(\mu + \omega_k) + \dots \tag{53}$$

The leading singular behaviour is encoded in the first term in (52).

To extract the singularity one can use the trivial identity

$$\ln(1 + z) = \int_0^\infty \mathrm{d}t \frac{\mathrm{e}^{-t}}{t}(1 - \mathrm{e}^{-zt}). \tag{54}$$

Now, the integration over $\mathrm{d}k$ in (52) can be performed exactly to give

$$\frac{1}{2\beta} \int \frac{\mathrm{d}k}{(2\pi)^3} \ln(\mu + \omega_k) = \frac{1}{2\beta} \ln(3 + \mu) + \frac{1}{2\beta} \int_0^\infty \mathrm{d}t(1 - I_0^3(t/(3 + \mu)))\frac{\mathrm{e}^{-t}}{t}. \tag{55}$$

Here $I_0$ is the modified Bessel function of the first kind. Now one can split the integration range as $[0, \infty) = [0, t_0] \cup [t_0, \infty)$. For $t_0$ large enough, by using the asymptotic behaviour of the Bessel function $I_0(t) \propto \mathrm{e}^t/\sqrt{2\pi t}$, one obtains

$$\int_0^\infty \mathrm{d}t(1 - I_0^3(t/(3 + \mu)))\frac{\mathrm{e}^{-t}}{t} = \int_0^{t_0} \mathrm{d}t(1 - I_0^3(t/(3 + \mu)))\frac{\mathrm{e}^{-t}}{t}$$
$$+ \int_{t_0}^\infty \mathrm{d}t(1 - \mathrm{e}^{3t/(3+\mu)}/(2\pi t/(3 + \mu))^{3/2})\frac{\mathrm{e}^{-t}}{t}. \tag{56}$$

The singularity of the free energy is extracted from the second term in (56). In the limit $\mu \to 0$ this gives

$$\int_{t_0}^{\infty} dt(1 - e^{3t/(3+\mu)}/(2\pi t/(3+\mu))^{3/2})\frac{e^{-t}}{t} = \Gamma(0, t_0) - \frac{\sqrt{3/2}}{(\pi t_0)^{3/2}} + \frac{\sqrt{3/2}(2t_0 - 1)}{2(\pi t_0)^{3/2}}\mu - \frac{\sqrt{2}}{3\pi}\mu^{3/2} + \cdots \tag{57}$$

Here $\Gamma(0, t_0)$ is the incomplete Gamma function. Note that both analytic and nonanalytic terms are present in (57). The term $\mu^{3/2}$ gives the well-known singularity of the free energy in the QSM [95]

$$f_{\text{sing}} = -\frac{\sqrt{2}}{6\pi}\mu^{3/2} \propto (g - g_c)^3, \quad \text{with } g > g_c. \tag{58}$$

From (58) we obtain $\nu = 1$. The prefactor of $(g - g_c)^3$ can be easily extracted from (57) and (38), (40). Equation (58) can be also derived by observing that the spherical constraint (see section 4.1) is obtained as $\partial f/\partial\mu = V$, and by integrating with respect to $\mu$ the singular contribution in (36). From (58), one has that the specific heat exponent $\alpha = 2 - d\nu = -1$ is negative. Equation (58) implies that the free energy and its first derivative with respect to $\beta$ and $g$ are continuous functions at the critical point.

We illustrate the behaviour of the free energy across the finite temperature transition in figure 5. In the two panels (a) and (b) we consider two different limits. Specifically, in (a) we calculate the free energy density from the finite-size expression (21), but using the value of $\mu$ calculated in the thermodynamic limit, i.e. by solving (30). This is convenient because it is straightforward to numerically solve (30), whereas solving (20) is a nontrivial task since the sum over $k$ cannot be performed explicitly. On the other hand, since in the thermodynamic limit one has $\mu = 0$ below the transition, the contribution of the zero mode in (21) is divergent and it has to be regularized by hand. The strategy that we use is to introduce a small mass putting $\mu = 10^{-6}$. While this ensures that one has the correct thermodynamic limit results, it affects the sub-leading contributions. This is clear from figure 5(a). In the figure we show data for $T = 0.6$ and several system sizes. The data for $L = 4$ show a jump at $g = g_c$ (vertical line). This is an artifact of the regularization. We checked that the jump becomes sharper and sharper as the mass term is sent to zero. At fixed mass, upon increasing $L$, the contribution of the zero-mode becomes negligible and the data approach the thermodynamic limit result (dashed-dotted line in the figure). Clearly, in the thermodynamic limit the free energy and its first derivative are continuous, as expected from (58). In figure 5(b) we show the free energy calculated by using the finite-size value of $\mu$, obtained by solving numerically (20). Now the contribution of the zero mode is finite because of the finite $L$.

### 4.4. Universal ratio $R_\xi$

One important goal of this paper is to investigate the effectiveness of entanglement-related observables to detect finite-temperature criticality. In this section we briefly review the behaviour of the universal ratio $\xi_{2\text{nd}}/L$, with $\xi_{2\text{nd}}$ the second-moment correlation length. This is a standard tool used in numerical simulations to analyse criticality [31]. For instance, it allows to detect second-order phase transitions via the so-called crossing method, and it can be used to extract the critical exponent $\nu$ by the usual data collapse analysis. The ratio $R_\xi$ is defined as
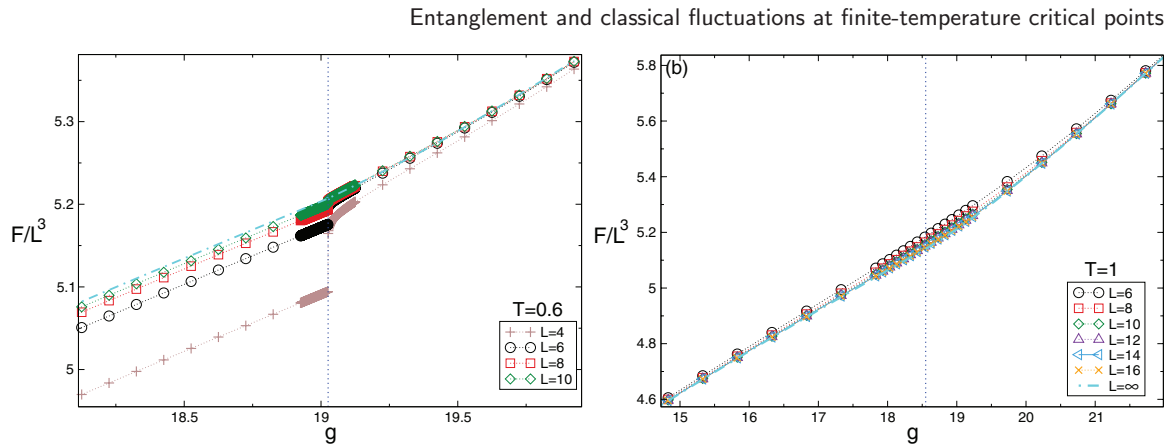
**Figure 5.** Density of free energy $F/L^3$ in the 3D quantum spherical model. (a) Results obtained by using the thermodynamic value of the spherical parameter $\mu$. $F/L^3$ is plotted versus the quantum coupling $g$. Data are for fixed temperature $T = 0.6$ and several system sizes $L$. The singular behaviour at the critical point (vertical dotted line) is unphysical (see the main text) and vanishes in the thermodynamic limit. The dashed-dotted line is the result in the thermodynamic limit. (b) The same as in (a) using the finite-size value of the spherical parameter $\mu$. Data are now for $T = 1$.

$$R_\xi = \frac{\xi_{2\mathrm{nd}}}{L}. \tag{59}$$

The so-called second-moment correlation length $\xi_{2\mathrm{nd}}$ is extracted from the long-distance behaviour of the correlation function. Its definition reads

$$\xi_{2\mathrm{nd}}^2 = \frac{\widetilde{G}(0)/\widetilde{G}(q_{\min}) - 1}{4\sin^2(\pi/L)}, \tag{60}$$

with $\widetilde{G}(k)$ the Fourier transform of the spin–spin correlation function (see (16) for the spherical model). In (60), $q_{\min}$ is the minimum nonzero lattice momentum $q_{\min} = (2\pi/L, 0, 0)$. Note that $\widetilde{G}(0)$ is the spin susceptibility $\chi$ defined as

$$\chi = \frac{1}{V}\sum_{n,m}\langle s_n s_m\rangle. \tag{61}$$

Alternatively, instead of $\xi_{2\mathrm{nd}}$, one can define $R_\xi$ by using $\xi_{\mathrm{gap}}$, which is defined from the gap between the ground state and the first excited state in the energy spectrum. For the QSM $R_\xi$ can be expressed analytically as a function of $\mu$. By using (16), one obtains that the correlation length is given as

$$\xi_{2\mathrm{nd}}^2 = \frac{1}{4\sin^2(\pi/L)}\left[\frac{\alpha_{2\pi/L}^2\coth(\beta E_{2\pi/L}/2)}{\alpha_0^2\coth(\beta E_0/2)} - 1\right]. \tag{62}$$

We now discuss the finite-size scaling properties of $R_\xi$. The finite-size scaling ansatz for $R_\xi$ reads as [31]

$$R_\xi = K((g - g_c)L^{1/\nu}). \tag{63}$$

Here we neglect both analytic and nonanalytic scaling corrections, that, however, one can include. The function $K(x)$ is universal apart from a renormalisation of its argument. Assuming analyticity of $K(x)$ one can expand (63) as

$$R_\xi = R_\xi^* + c_1(g - g_c)L^{1/\nu} + \dots . \tag{64}$$

The value $R_\xi^*$ depends only on the universality class of the transition and on the geometry (for instance, the boundary conditions). Crucially, equation (64) implies that the curves for $R_\xi$ at different finite sizes $L$ exhibit a crossing at the critical point. Moreover, when plotted against the scaling variable $X \equiv (g - g_c)L^{1/\nu}$, the data for different $L$s collapse on the same curve, at least in the limit $L \to \infty$, when corrections to scaling can be neglected.

It is important to understand the behaviour of $R_\xi$, especially with the moderately small system sizes that are available in our simulations. In figure 6 we show numerical data for $R_\xi$ plotted as a function of $g$. The data are for $T = 1$. The curves for different $L$ exhibit a crossing at $g \approx g_c$, as expected. The value $R_\xi^* \approx 0.5$ at the crossing is universal, and it could be calculated by using the results of [97]. To our knowledge $R_\xi^*$ is not known exactly. Note that scaling corrections are present. Indeed, for the smaller $L$s the crossing is not at $g_c$ (vertical line). Upon increasing $L$, the crossing point exhibits a systematic drifts towards $g_c$. In figure 7 we show the same data as in figure 6, now plotted versus the scaling variable $X = (g - g_c)L^{1/\nu}$. As expected, due to the scaling corrections, the smaller lattice sizes do not show data collapse. However, upon increasing $L$ the quality of the collapse improves significantly. The scaling is satisfactory for the larger sizes. In the inset we provide data also for $T = 2.2$. We observe that scaling corrections are smaller as compared with $T = 1$, which is reflected in a better data collapse. Note that the scaling function $K$ (see (63)) depends on the temperature, although the value at $X = 0$ is the same for both temperatures, as expected. However, since the finite-temperature universality class is the same on the whole para-ferro transition line (see figure 2), the two scaling functions should coincide after an analytic redefinition of the scaling field $u_1$ as $u_1 \approx c_T(g - g_c)$, where $c_T$ depends on the temperature. We numerically verified that $c_{T=2.2}/c_{T=1} \approx 1/2$.

## 5. Entanglement scaling in the critical spherical model

We now discuss the behaviour of entanglement-motivated quantities in the finite-temperature critical QSM. Specifically, in section 5.1 we briefly review how to calculate entanglement-related observables. In section 5.2 we focus on the von Neumann entropy. In section 5.3 we discuss the von Neumann and Rényi mutual information. In section 6 we investigate the logarithmic negativity. We consider both the negativity between two spins in an infinite system (in section 6.1), as well as the negativity between two extended adjacent blocks (in section 6.2). Finally, in section 7 we focus on the single-particle entanglement spectra and negativity spectra.
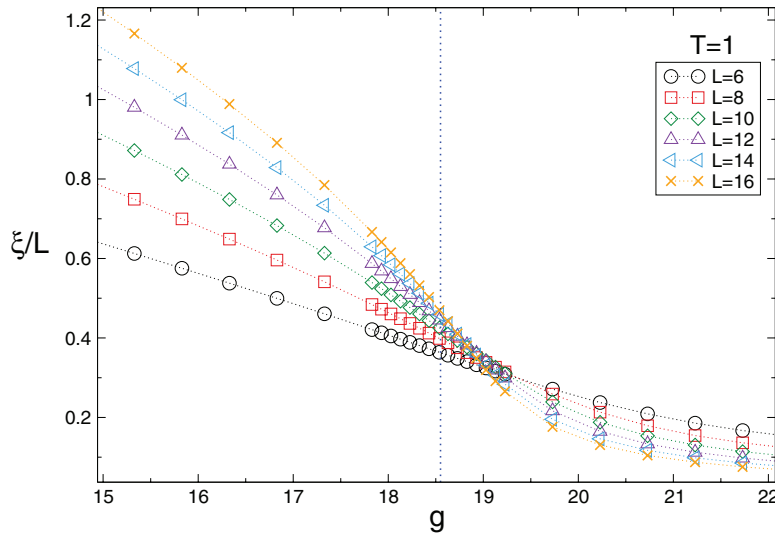
**Figure 6.** Scaling of the second-moment correlation length at a finite-temperature phase transition in the QSM. Rescaled correlation length $\xi_{2\mathrm{nd}}/L$, with $L$ the system size, plotted as a function of $g$. The data are for fixed $T = 1$ and several $L$. The vertical dotted line marks the critical point at $g_c \approx 18.52$. Note the crossing at $g \approx g_c$ between curves for different system sizes.
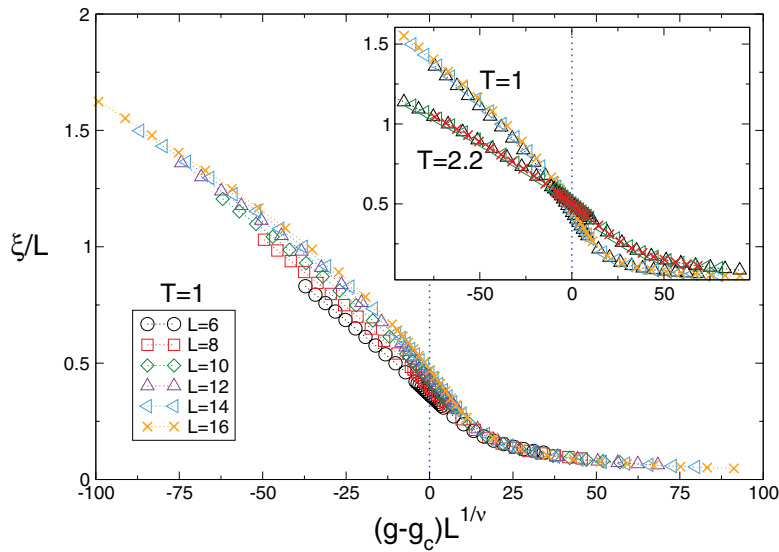


**Figure 7.** Same data as in figure 6 plotted versus the scaling variable $X \equiv (g - g_c)L^{1/\nu}$, with $\nu = 1$. Upon increasing $L$, the data for different $L$ collapse on the same curve. Note the large scaling corrections near the critical region at $X = 0$. Inset: zoom around $X = 0$ showing only data for $L = 12$–$16$. We now show results also for $T = 2.2$. Note for both temperatures the same universal value $\xi_{2\mathrm{nd}}/L \approx 0.5$ at the critical point $X = 0$.

## 5.1. Computation of entanglement-related observables in the QSM

The QSM is mappable to a system of free bosons (see section 3). This implies that entanglement-related quantities are obtained from the two-point correlation functions (see [100] for a review). The key ingredients are the matrices $\mathbb{Q}_{nm} \equiv \langle s_n s_m \rangle$ and $\mathbb{P}_{nm} \equiv \langle p_n p_m \rangle$ constructed from the two-point correlation functions (see (16) and (17)).

Let us define the matrices $\mathbb{Q}[A]$ and $\mathbb{P}[A]$, where $n, m$ are now restricted to subsystem $A$ (see figures 1(b) and (c)). The Rényi entropies of $A$ are constructed from the eigenvalues $\lambda_j^2$ of the matrix $\mathbb{Q}[A] \cdot \mathbb{P}[A]$. As it is common in the literature, we refer to the $\lambda_j$ as the single-particle entanglement spectrum levels. In terms of $\lambda_j$, the Rényi entropies are given as

$$S_{n,A} = -\frac{1}{1-n} \sum_j \ln \left[ \left( \lambda_j + \frac{1}{2} \right)^n - \left( \lambda_j - \frac{1}{2} \right)^n \right].$$
(65)

The von Neumann entropy is obtained by performing the analytic continuation $n \to 1$, which yields

$$S_{\mathrm{vN}} = \sum_j \left[ \left( \lambda_j + \frac{1}{2} \right) \ln \left( \lambda_j + \frac{1}{2} \right) - \left( \lambda_j - \frac{1}{2} \right) \ln \left( \lambda_j - \frac{1}{2} \right) \right].$$
(66)

The mutual information (see section 2) is obtained by using (65), (66) and (4).

We now discuss the logarithmic negativity for a partition of $A$ as $A = A_1 \cup A_2$ (see figure 1(c)). One first defines the transposed matrix $\mathbb{P}[A^{T_2}]$ as

$$\mathbb{P}[A^{T_2}] \equiv \mathbb{R}[A^{T_2}] \mathbb{P}[A^{T_2}] \mathbb{R}[A^{T_2}].$$
(67)

Here the matrix $\mathbb{R}[A^{T_2}]$ acts as the identity matrix $\mathbb{I}_{A_1}$ on $A_1$ and as $-\mathbb{I}_{A_2}$ on $A_2$. The eigenvalues $\nu_i^2$ of $\mathbb{Q}[A] \cdot \mathbb{P}[A^{T_2}]$ form the single-particle negativity spectrum. In terms of $\nu_i^2$, the negativity is given as

$$\mathcal{E} = \sum_i \max(0, -\ln(2\nu_i)).$$
(68)

Note that while $\nu_i^2 > 0$, $-\ln(2\nu_i)$ can be both positive and negative.

## 5.2. Von Neumann entropy

Let us start discussing the behaviour of the von Neumann entropy. Numerical data for the half-system entropy are reported in figure 8, for fixed temperature $T = 2.2$. Similar to the free energy (see figure 5) and to the thermal entropy, the von Neumann entropy exhibits a volume law at any $g$. The figure shows the density of entropy $S_{\mathrm{vN}}/L^3$, plotted as a function of $g$. Different symbols are for different system sizes. Finite-size effects decay very quickly with $L$. The data for the larger sizes $L = 12$–$16$ collapse on the same curve. The entropy density exhibits regular behaviour around the transition. This is expected because at finite temperature the density of von Neumann entanglement entropy becomes the same as the thermal entropy, which is not singular at the transition. We should stress, however, that sub-leading contributions can be singular, for instance due to the presence of the zero mode. A natural scaling ansatz for the entropy density reads as
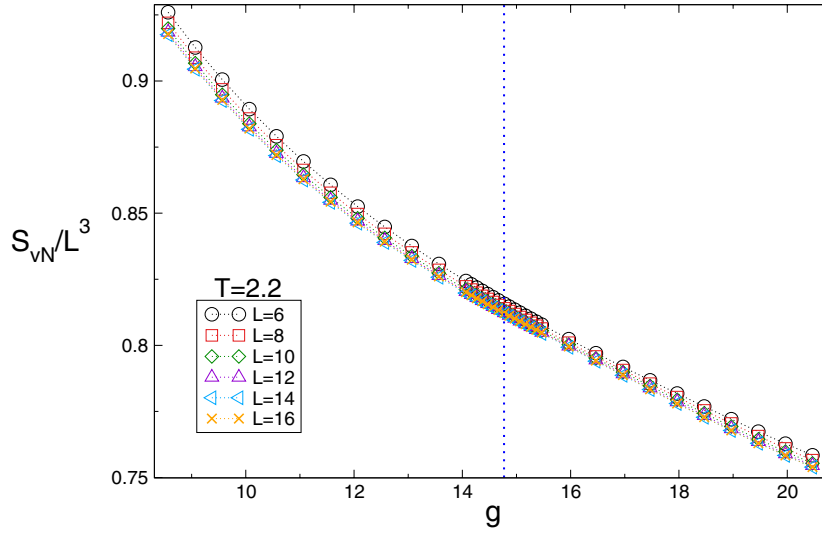
**Figure 8.** Scaling of the entanglement entropy density $S_{\mathrm{vN}}/L^3$ at a finite-temperature phase transition in the quantum spherical model. The figure shows $S_{\mathrm{vN}}/L^3$ as a function of $g$ for several system sizes $L$. The vertical line marks the critical point.

$$\frac{S_{\mathrm{vN}}}{L^3} = L^{-3} s_{\mathrm{sing}}((g - g_c)L^{1/\nu}) + s_{\mathrm{an}}(g). \tag{69}$$

Here the functions $s_{\mathrm{sing}}$ and $s_{\mathrm{an}}$ encode the singular and regular terms. In (69) we neglect scaling corrections. Equation (69) implies that the singular term vanishes at the transition when increasing $L$, and only the regular term survives. We should stress that in (69) we also neglect logarithmic contributions that can arise because of the presence of the zero mode [39], which reflects the symmetry breaking. We will investigate these contributions in section 7 discussing the single-particle entanglement spectrum. Moreover, in principle, there can be extra logarithmic corrections if the bipartition has corners (see, for instance [30]). These are not present in our case because the boundary between $A$ and its complement is smooth (see figure 1).

## 5.3. Mutual information

We now turn to the mutual information (see (4) for its definition). Here we consider a bipartite system at finite temperature (as in figure 1(b)). The system is divided into two equal parts $A$ and $B = \bar{A}$. We consider the mutual information between $A$ and its complement. As it is clear from (4), the volume-law contribution of the entropies cancels out. This cancellation happens for any value of $g$ and $T$. Thus, the mutual information exhibits an area law. A natural scaling ansatz for the density of the mutual information is

$$\frac{I_n}{L^2} = L^{-2} q_{\mathrm{sing}}^{(n)}((g - g_c)L^{1/\nu}) + q_{\mathrm{an}}^{(n)}(g). \tag{70}$$

Equation (70) is compatible with the scaling ansatz proposed in [25]. Here $\nu$ is the critical exponent as in (69). Similar to (69), here we are neglecting scaling corrections. In (70), $q_{\mathrm{an}}$ is the analytic contribution.

We present our results for the von Neumann mutual information $I_{\mathrm{vN}}$ in figure 9. We plot the density of mutual information $I_{\mathrm{vN}}/L^2$ versus $g$. Data are at fixed $T = 2.2$. The data exhibit a crossing point around $g \approx 13.5$, which is incompatible with the critical point at $g_c \approx 14.77$. Moreover, the position of the crossing point does not change upon increasing system size, in contrast with the behaviour of $R_\xi$ (see figure 6). Importantly, the curves for different $L$s do not 'fan out' as $L$ increases, in contrast with the behaviour for the ratio $R_\xi$ (see figure 6). As for the von Neumann entropy, the mutual information is dominated by the regular part (see (70)). More precisely, although the singular term in (70) gives a universal crossing, this is not visible because it is suppressed as $L^{-2}$ in the limit $L \to \infty$.

Similar behaviour is observed for the Rényi mutual information. This is discussed in figure 10 focusing on $I_2$. As for $I_{\mathrm{vN}}$, the data in figure 10 collapse on the same curve upon increasing $L$. Specifically, in the paramagnetic phase for $g > g_c$ and close to the critical point, finite-size effects decay dramatically with $L$, and the data with $L \gtrsim 10$ are already indistinguishable from the thermodynamic limit. Also no universal crossing is visible within the system sizes presented in the figure.

It is interesting to compare our results with [25] (see also [26]). There is large evidence, based on quantum Monte Carlo simulations, that at a finite-temperature phase transition the ratio $I_2/L^{d-1}$ exhibits two crossing at $T_c$ and $2T_c$, with $T_c$ the critical temperature. The scaling ansatz for the mutual information presented in [25] is compatible with (70). However, as stressed in [25] the presence of the crossing relies on $q_{\mathrm{an}}^{(n)}$ changing sign across the phase transition. Our results suggest that this does not happen in the QSM.

## 6. Logarithmic negativity

We now discuss the logarithmic negativity between two complementary subsystems. This allows us to study the interplay between genuine quantum fluctuations and thermal fluctuations. One of the goals of this section is to map out the role of entanglement in the different regions of the phase diagram of the QSM.

The generic behaviour of the negativity is illustrated in figure 11. The figure shows a density plot of $\mathcal{E}$ as a function of $g$ and $T$. The dashed-dotted line is the critical line dividing the paramagnetic phase from the ordered phase (see figure 2). In the figure we show the half-system negativity for a cube of linear size $L = 2$. The data are obtained by using the value of $\mu$ in the thermodynamic limit and the finite-size formulas for the correlators (see (16) and (17)). The negativity is large at the quantum critical point and in the ordered phase, and it quickly decays upon increasing the temperature. The dotted line is the negativity 'death line'. Above the death line the half-system negativity is exactly zero. The death line that we report in the figure is obtained by considering the half-system negativity in the limit $L \to \infty$. In the figure we also report the death line calculated from the negativity between two adjacent sites embedded in an infinite
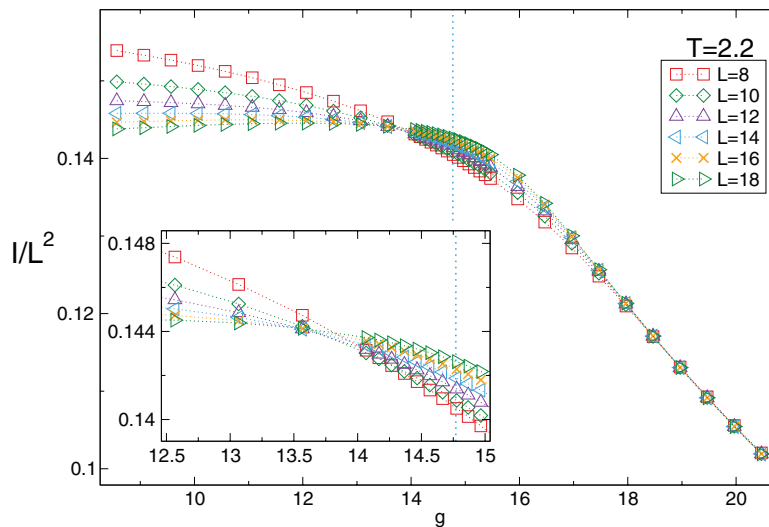
**Figure 9.** Scaling of the density of von Neumann mutual information $I_{\text{vN}}/L^2$ at a finite-temperature phase transition in the quantum spherical model: $I_{\text{vN}}/L^2$ as a function of $g$ for several system sizes $L$. Data are for fixed $T = 2.2$. The vertical dotted line marks the critical point at $g_c$. Note the spurious crossing at $g < g_c$.
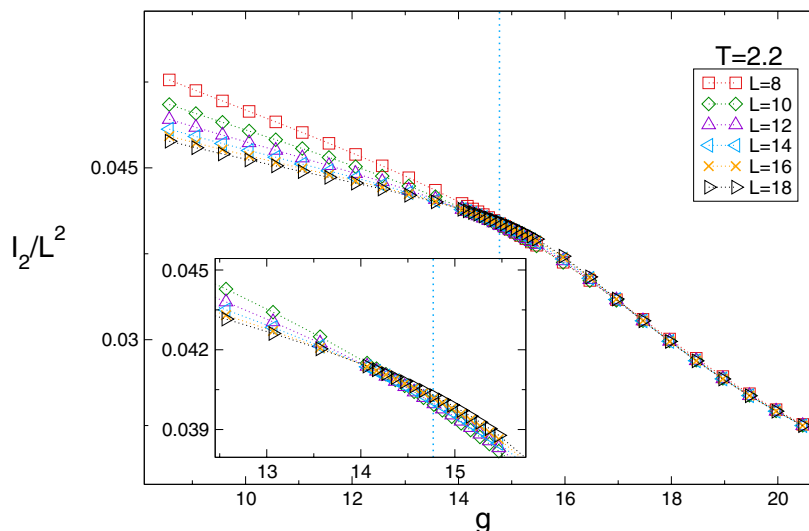


**Figure 10.** Scaling of the density of Rényi mutual information $I_n/L^2$ with $n = 2$ at a finite-temperature phase transition: $I_n/L^2$ as a function of $g$ for several system sizes $L$. Data are for fixed $T = 2.2$. The vertical dotted line marks the critical point at $g_c$. Inset: zoom around the critical region. Note that no crossing is present.

system (continuous line), which provides only a bound. Interestingly, the death line exhibits the behaviour $\propto g^{1/2}$ at small $g$. For the case of two sites embedded in the infinite system the precise behaviour can be calculated analytically and it is reported in the figure (dashed line). Finally, it is interesting to observe that the death line increases with $g$, although the negativity decreases as $1/g$ (see section 6.1.1).
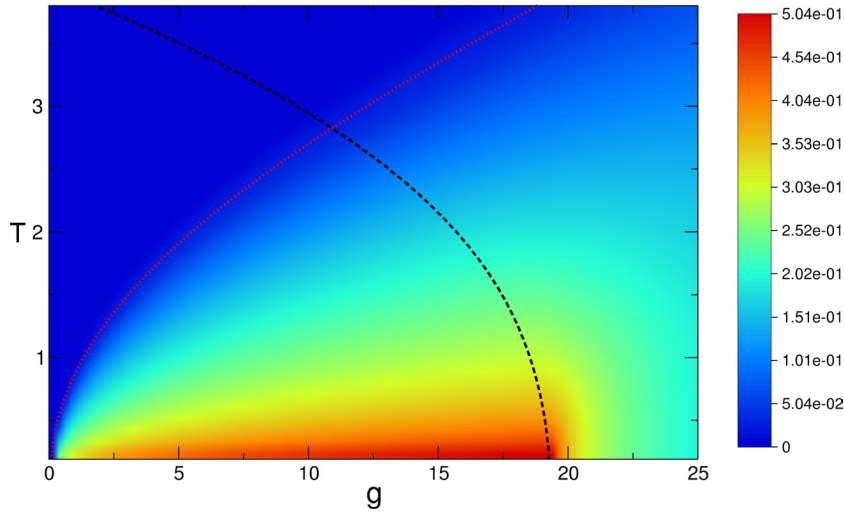
**Figure 11.** Survey of the behaviour of the logarithmic negativity in the QSM. On the $x$-axis $g$ is the quantum coupling. On the $y$-axis $T$ is the temperature. The figure shows the density plot of the half-system negativity. The system is a cube of length $L = 2$. The dashed-dotted line is the critical line dividing the paramagnetic phase from the ordered phase at low temperature. The dotted line is the 'death line' of the negativity. Above the death line the negativity is exactly zero. The continuous line is the death-line calculated from the negativity between two adjacent spins embedded in an infinite system. The behaviour as $\propto g^{1/2}$ at small $g$ is also reported (dashed line).

### 6.1. Two-site negativity

Several of the generic features of the negativity discussed in figure 11 can be extracted by considering two adjacent spins embedded in an infinite system. In this section we derive analytically the behaviour of the logarithmic negativity in this situation.

*6.1.1. Large g expansion.* It is straightforward to derive the behaviour of the negativity between the two sites in the large $g$ regime (see figure 2). The starting point of the analysis are the correlators $\langle s_n s_m \rangle$ and $\langle p_n p_m \rangle$ in the large $g$ limit. These are reported in (26) and (27). Now the matrices $\mathbb{Q}[A]$ and $\mathbb{P}[A^{T_2}]$ (see section 2 for their definitions) are two-by-two matrices. The negativity spectrum contains only two levels. These are the eigenvalues $\nu_\pm^2$ of $\mathbb{Q}[A] \cdot \mathbb{P}[A^{T_2}]$, which in the large $g$ limit are given as

$$\nu_\pm = \frac{g \pm 2}{2g}. \tag{71}$$

Since $\nu_+ > 1/2$, only $\nu_-$ contributes to the negativity (see (68)), which is given as

$$\mathcal{E} = -\ln\left(\frac{g-2}{g}\right). \tag{72}$$

By expanding in the large $g$ limit, one obtains the behaviour $\mathcal{E} \propto 1/g$.

*6.1.2. Low-temperature expansion.* It is also interesting to discuss the limit of low-temperature in the ordered phase of the QSM. To do that, we exploit the expansion of the correlators $\langle s_n s_m \rangle$ and $\langle p_n p_m \rangle$ (see (28) and (29)). Let us first consider the negativity

between site $n \equiv (n_x, n_y, n_z)$ and $m \equiv (m_x, m_y, m_z)$. The eigenvalues $\nu_i^2$ of $\mathbb{Q}[A] \cdot \mathbb{P}[A^{T_2}]$ are given as

$$\nu_1^2 = \frac{(W_n'' - W_m'')(\sqrt{2} + 3(W_n' + W_m')\beta^2 g)}{12\beta^2 g}, \tag{73}$$

$$\nu_2^2 = \frac{(W_n' - W_m')(\sqrt{2}\pi^2 + 15(W_n'' + W_m'')\beta^4 g)}{60\beta^4 g^2}. \tag{74}$$

Here we defined the Watson-type integrals as

$$W_n' \equiv \int \frac{\mathrm{d}k}{(2\pi)^3} \mathrm{e}^{\mathrm{i}kn} \frac{1}{\sqrt{\omega_k}}, \quad W_n'' \equiv \int \frac{\mathrm{d}k}{(2\pi)^3} \mathrm{e}^{\mathrm{i}kn} \sqrt{\omega_k}. \tag{75}$$

Here $\omega_k$ is defined in (12). Interestingly, the integral $W_n'$ can be calculated analytically in terms of hypergeometric functions [98]. We now restrict ourselves to the negativity between two nearest-neighbour spins, i.e. with $|n - m| = 1$. Specifically, we choose $n = (0, 0, 0)$ and $m = (1, 0, 0, )$. One can numerically check that $\nu_1^2 < 1/4$, implying that $\nu_1$ does not contribute to the negativity (see (68)). On the other hand, for a given $\beta$, one has that $\nu_2$ contributes to the negativity only for sufficiently large $g$. Specifically, we observe that the condition $g > g^*(\beta)$ has to hold, with the 'critical' value $g^*$ given as

$$g^* = \frac{2^{1/4}\pi\sqrt{W_0' - W_1'}}{\sqrt{15}\beta^2\sqrt{1 - (W_0' - W_1')(W_0'' + W_1'')}}, \tag{76}$$

where $W_0' \equiv W_{(0,0,0)}'$, $W_1' \equiv W_{(1,0,0)}'$, and similarly for $W''$. For each value of temperature, the negativity is exactly zero for $g < g^*(T)$. Note in (76) the behaviour $g^* \propto 1/\beta^2$. This behaviour persists when considering the negativity between two extended systems, although the prefactor in (76) is different. In particular, for two extended systems one obtains a larger value of $g^*$ in (76), as it is clear from figure 11.

Note that for large enough temperature the negativity vanishes even on the critical line (see figure 2). This is shown explicitly in figure 12. The figure shows $\mathcal{E}$ calculated on the critical line $T_c(g)$, with $T_c$ the critical temperature at the given value of $g$. The negativity is exactly zero for $g \lesssim 14$, whereas it is finite nonzero up to $g \approx 19$, which corresponds to zero temperature.

The behaviour of the negativity between two nearest-neighbour sites as a function of both temperature and quantum coupling $g$ is summarized in figure 13. Panel (a) shows $\mathcal{E}$ versus $g$, at fixed $T = 1$. In the figure we plot the negativity and not its density. The vanishing behaviour below $g^* \approx 2$, as predicted by equation (76), is clearly visible, as well as the slow decay as $1/g$ in the paramagnetic phase. Panel (b) shows $\mathcal{E}$ at fixed $g = g_c(T = 1)$ as a function of $T$. The negativity exhibits a weak dependence on temperature in the ordered phase, whereas it suddenly drops to zero in the paramagnetic phase (sudden death).

*6.1.3. Critical region.* An important feature in figure 13(a) is that the negativity exhibits regular behaviour across the para-ferro transition. On the other hand, recently it has been observed that the negativity can exhibit a cusp-like singularity at a finite
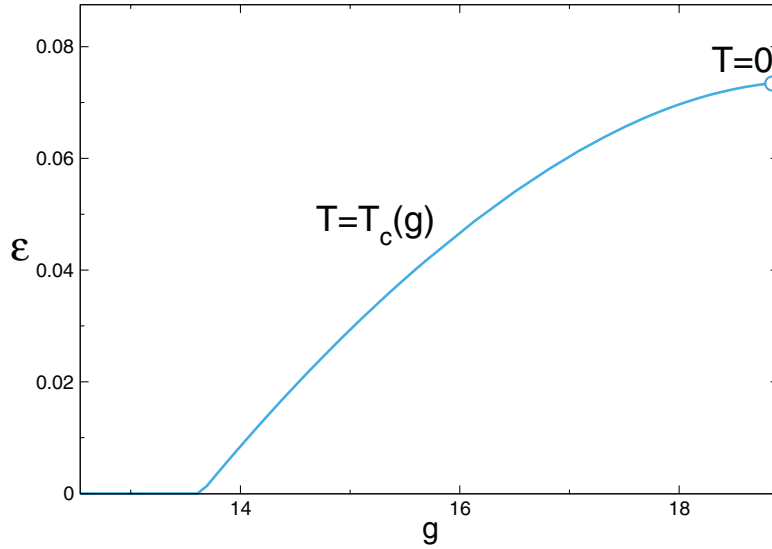
**Figure 12.** Logarithmic negativity between two nearest-neighbour spins embedded in an infinite system. We show $\mathcal{E}$ along the critical $T = T_c(g)$ line of the para-ferro transition. Note the sudden death of the negativity at $g \approx 13.6$.

temperature phase transition [16, 17]. Moreover, it has been suggested that the singular part of the negativity obeys the scaling form as

$$\mathcal{E}_{\text{sing}} \propto |g - g_c|^{1-\alpha}, \tag{77}$$

with $\alpha$ the specific heat critical exponent. Our results are consistent with [16, 17]. Specifically, for the $3D$ QSM one has $\alpha = -1$. Thus, equation (77) predicts that $\mathcal{E}_{\text{sing}}$ has a singular term $(g - g_c)^2$, i.e. a weaker than a cusp singularity. On the other hand, for $\alpha = 0$, which is the case investigated in [17], one has the cusp-like behaviour as $\mathcal{E}_{\text{sing}} \propto |g - g_c|$.

To clarify the behaviour of $\mathcal{E}$ for two nearest-neighbour sites, it is useful to consider the single-particle negativity spectrum. Using the expansions for the correlators near the critical point (see (42)–(45)), it is straightforward to obtain the spectrum levels. These are given as
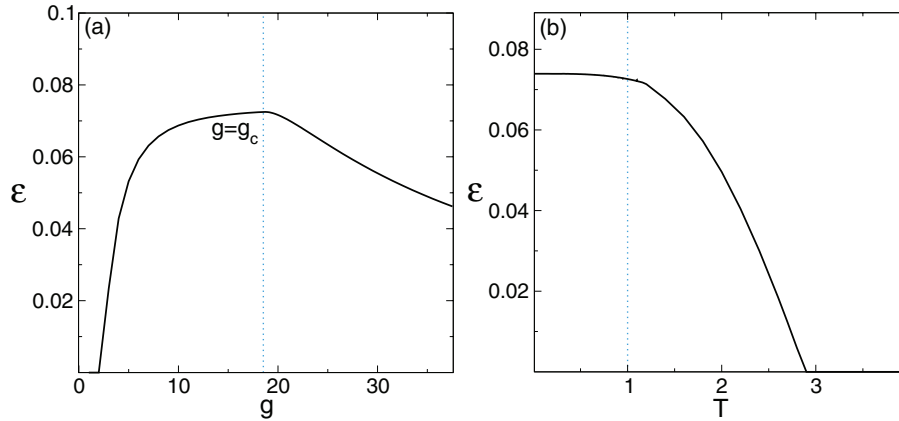
$$\nu_1^2 = (S_{nn}^{(0)} - S_{nm}^{(0)})(P_{nn}^{(0)} + P_{nm}^{(0)}) \\ + \left[(S_{nn}^{(1)} - S_{nm}^{(1)})(P_{nn}^{(0)} + P_{nm}^{(0)}) + (S_{nn}^{(0)} - S_{nm}^{(0)})(P_{nn}^{(1)} - P_{nm}^{(1)})\right](g - g_c), \tag{78}$$

$$\nu_2^2 = (S_{nn}^{(0)} + S_{nm}^{(0)})(P_{nn}^{(0)} - P_{nm}^{(0)}) \\ + \left[(S_{nn}^{(1)} + S_{nm}^{(1)} + 2Z_{\text{sing}})(P_{nn}^{(0)} - P_{nm}^{(0)}) + (S_{nn}^{(0)} + S_{nm}^{(0)})(P_{nn}^{(1)} + P_{nm}^{(1)})\right](g - g_c). \tag{79}$$

Here we defined

$$S_{nm}^{(0)} \equiv \frac{\sqrt{g_c}}{2\sqrt{2}} \int \frac{\mathrm{d}k}{(2\pi)^3} \frac{\coth(\beta\sqrt{g_c\omega_k/2})}{\sqrt{\omega_k}} \mathrm{e}^{\mathrm{i}k(n-m)} \tag{80}$$

$$S_{nm}^{(1)} \equiv \int \frac{\mathrm{d}k}{(2\pi)^3} \left(\frac{\beta}{8} + \frac{\coth(\beta\sqrt{g_c\omega_k/2})}{4\sqrt{2g_c\omega_k}} - \frac{\beta}{8}\coth^2(\beta\sqrt{g_c\omega_k/2})\right)\mathrm{e}^{\mathrm{i}k(n-m)} \tag{81}$$

**Figure 13.** Logarithmic negativity between two adjacent spins in the quantum spherical model: negativity $\mathcal{E}$ plotted as a function of $g$ (in (a)) and of the temperature $T$ (in (b)). The figure shows results in the thermodynamic limit. The vertical lines denote the critical point. Data in (a) are for fixed $T = 1$. In (b) we fixed $g = g$ ($T_c = 1$) (see figure 2). Note in (a) the slow decay at $g \to \infty$ and the 'death' of $\mathcal{E}$ at $g \to 0$. Note that in (b) the negativity is identically zero for $T \gtrsim 3$.

$$P_{nm}^{(0)} \equiv \frac{1}{\sqrt{2g_c}} \int \frac{\mathrm{d}k}{(2\pi)^3} \coth(\beta\sqrt{g_c\omega_k/2})\sqrt{\omega_k}\mathrm{e}^{\mathrm{i}k(n-m)} \tag{82}$$

$$P_{nm}^{(1)} \equiv \frac{1}{g_c} \int \frac{\mathrm{d}k}{(2\pi)^3}\omega_k\Big(\frac{\beta}{4} - \frac{\coth(\beta\sqrt{g_c\omega_k/2})}{2\sqrt{2g_c\omega_k}} - \frac{\beta}{4}\coth^2(\beta\sqrt{g_c\omega_k/2})\Big)\mathrm{e}^{\mathrm{i}k(n-m)} \tag{83}$$

$$Z_{\mathrm{sing}} \equiv 2\sqrt{2}\pi\beta \int \frac{\mathrm{d}k}{(2\pi)^3}\Big(\frac{\beta}{8} + \frac{\coth(\beta\sqrt{g_c\omega_k/2})}{4\sqrt{2g_c\omega_k}} - \frac{\beta}{8}\coth^2(\beta\sqrt{g_c\omega_k/2})\Big). \tag{84}$$

Note that $Z_{\mathrm{sing}}$ contains the singular term $\sqrt{\mu}$ that we derived in section 4.1. Interestingly, this affects only $\nu_2$, whereas $\nu_1$ is regular.

In figure 14 we show the levels of the single-particle negativity spectrum (see (80) and (81)). In the figure we plot $-\ln(2\nu_n)$ versus $g$. In (a) we show the regular eigenvalue $\nu_1$, whereas $\nu_2$ is reported in (b). The singularity as $|g - g_c|$ in (b) is clearly visible. Importantly, one has that $-\ln(2\nu_2) < 0$, implying that $\nu_2$ does not contribute to the logarithmic negativity. This suggests that in the case of two extended subsystems only a subset of the single-particle negativity spectrum levels will exhibit singular behaviour. These levels, however, do not contribute to the negativity, which is regular at the finite-temperature transition. This point will be better clarified when we will discuss the negativity spectrum of two extended regions in section 7.

## 6.2. Half-system negativity

We now discuss the half-system logarithmic negativity. Our results are reported in figure 15. The figure provides an overview of $\mathcal{E}$ at fixed temperature $T = 1$ and $T = 0.2$ ((a) and (b), respectively) as a function of $g$. In both panels we plot the negativity density $\mathcal{E}/L^2$ of the half system. The different lines are for different sizes $L$. Similar to
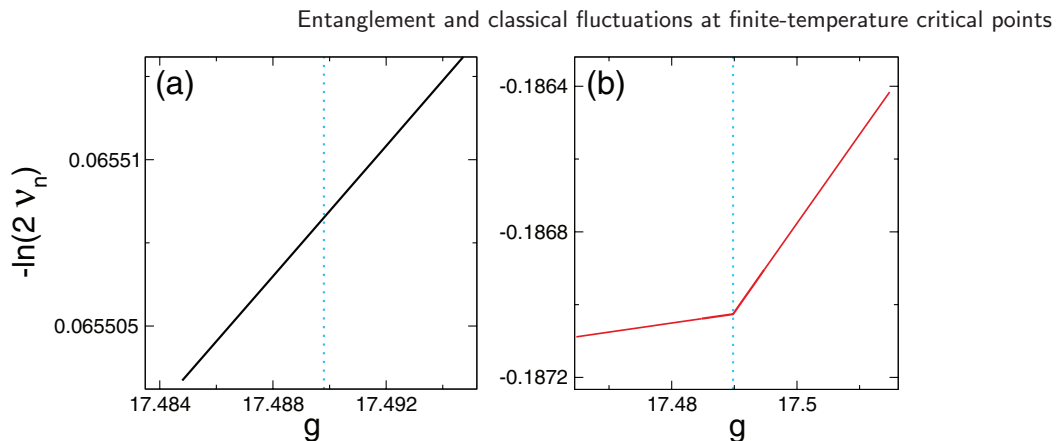
**Figure 14.** Single-particle negativity spectrum for two adjacent spins embedded in an infinite system. We plot $-\ln(2\nu_n)$, with $\nu_n^2$ the eigenvalues of the correlation matrix, versus $g$. Data are for fixed $T \approx 1.486$. The spectrum consists of two eigenvalues shown in (a) and (b). Note that in (b) $-\ln(2\nu_n) < 0$, implying that the level does not contribute to the negativity. Note the kink at the critical point (vertical line). In contrast, the eigenvalue in (a) is regular, implying that the negativity is not singular at the critical point.

section 4.3, we calculate the negativity by using the finite-size result for the correlators (see (16) and (17)), and the value of the spherical parameter $\mu$ in the thermodynamic limit. To regularize the divergent contribution of the zero mode we fix $\mu = 10^{-6}$ for $g \leqslant g_c$. We also checked that the results for the negativity do not depend on the choice of the regularization.

Clearly, in figure 15 finite-size effects are small, especially for $T = 1$ (see (a)). In (a) the data for $L = 8$ cannot be distinguished from the result in the thermodynamic limit. In both (a) and (b), the negativity has its maximum value at the critical point. In the paramagnetic phase the negativity decays as $1/g$, similar to the case of two spins (see section 6.1). Within the ordered phase $\mathcal{E}$ exhibits a mild dependence on $g$, except at small $g$, where it drops dramatically. Specifically, for $g < g^* \approx 2$ the negativity is exactly zero. Note that $g^*$ decreases with decreasing the temperature (compare (a) and (b) in the figure). This behaviour is similar to what observed for the two-site negativity (see figure 13). Again, this implies that for any value of the temperature there is a 'critical' value of the coupling $g$ below which the quantum fluctuations are not strong enough to give a finite entanglement negativity. An important remark, however, is that since the negativity gives only a bound on the entanglement, the vanishing of $\mathcal{E}$ below $g^*$ does not imply the absence of entanglement. From figure 15(a) it is clear that at $T = 1$, the negativity exhibits regular behaviour at $g_c$. On the other hand, upon decreasing the temperature the negativity develops a cusp. This is clear from figure 15(b). Similar (weak) singular behaviour was observed in the area-law prefactor of the von Neumann entropy in ground-state quantum phase transitions [27, 33, 34].

It is interesting to investigate the behaviour of the logarithmic negativity at fixed $g$, i.e. approaching criticality by changing the temperature. This is illustrated in figure 16. We plot $\mathcal{E}/L^2$ versus $T$ for fixed $g = g_c(T = 1)$. Now the negativity exhibits a fast decay with $T$ in the paramagnetic region, and already for $T \approx 3$ it is exactly zero. This is in contrast with the result at fixed $T$ (see figure 15), where the behaviour as $1/g$ is observed. Finite-size effects are larger upon decreasing the temperature in the ordered
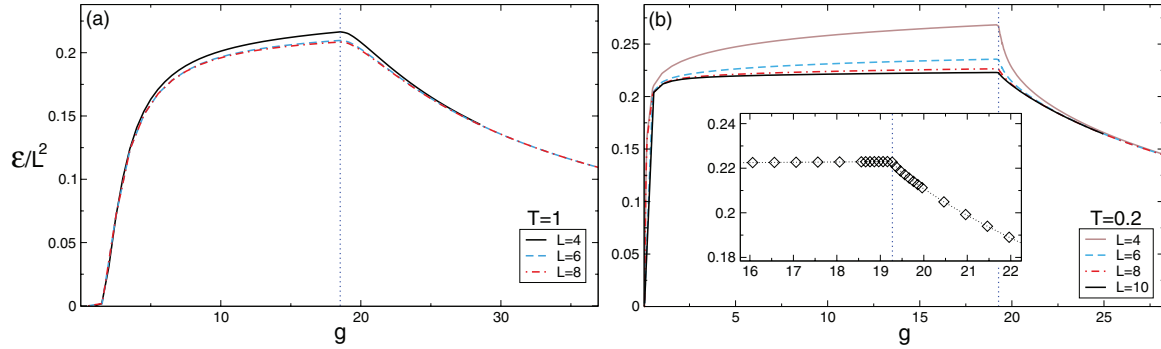
**Figure 15.** Logarithmic negativity in the finite-temperature quantum spherical model. (a) and (b) Show the negativity density $\mathcal{E}/L^2$ plotted versus the quantum coupling $g$ for $T=1$ and $T=0.2$, respectively. Data are obtained by using the thermodynamic result for the spherical constraint $\mu$. The effect of the system size $L$ is small, especially for $T=1$. The qualitative behaviour is similar to figure 13 (compare (a) and (b)). For $T=1$ the negativity exhibits regular behaviour at $g_c$, whereas in the limit $T \to 0$ a cusp-like feature appears at $g_c$. In (b) the inset shows the data for $L=10$, zooming around the critical point.

phase. Note that for the smaller system sizes one has a quite large value of $\mathcal{E}$ in the limit $T \to 0$, although the area-law behaviour $\mathcal{E} \propto L^2$ is expected to hold also at zero temperature. Finally, the negativity is not singular at the critical point, as in figure 15.

Finally, we investigate the behaviour of the logarithmic negativity in finite-size systems. To address this point, we provide results for the half-system negativity obtained by using the finite-size value of the spherical parameter $\mu$, i.e. by numerically solving (20). Our results are reported in figure 17. The figure plots the negativity density $\mathcal{E}/L^2$ versus $g$, for several sizes (symbols in the figure). Similar to the mutual informations (see figures 9 and 10), the data show small finite-size effects both in the paramagnetic phase and in the ordered phase. At the critical point (vertical line) finite-size effects are larger. However, the data appear to converge to the thermodynamic limit result (dashed-dotted line). The latter is obtained from figure 15. Note that the data for different $L$s do not exhibit any crossing at the critical point.

## 7. Entanglement spectra, negativity spectra, and the zero mode

In section 6.1.3 we showed that the negativity spectrum for two nearest-neighbour sites contains one regular and one singular levels. The latter exhibits a cusp-like singularity across the finite temperature transition. The singular level, however, does not contribute to the logarithmic negativity. Moreover, we observed in section 6.2 that the negativity between two extended blocks shows regular behaviour across the transition, similar to the entanglement entropy (see figure 8). It is interesting to investigate how this is reflected in the negativity spectrum of two extended regions. It is also interesting to compare the singularity structure of the negativity spectrum and the entanglement spectrum.
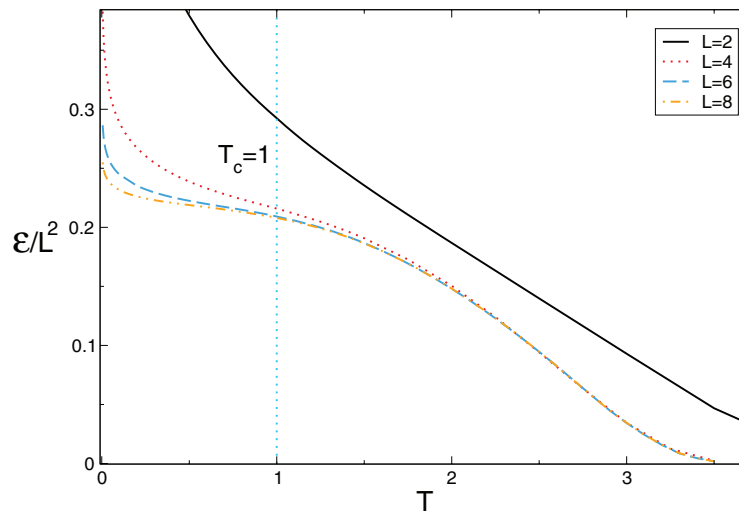
**Figure 16.** Density of the logarithmic negativity $\mathcal{E}/L^2$ in the 3D QSM at fixed $g_c \approx 18.52$ plotted as a function of temperature $T$. Data are obtained by using the value of the spherical parameter $\mu$ in the thermodynamic limit. The vertical line is the critical temperature $T_c = 1$ at $g_c$ (see figure 2). Note that $\mathcal{E} = 0$ for $T \gtrsim 3.5$. In the limit $T \to 0$ quantum fluctuations are enhanced and $\mathcal{E}/L^2$ increases, although area-law $\mathcal{E} \propto L^2$ behaviour should persist even at zero temperature.
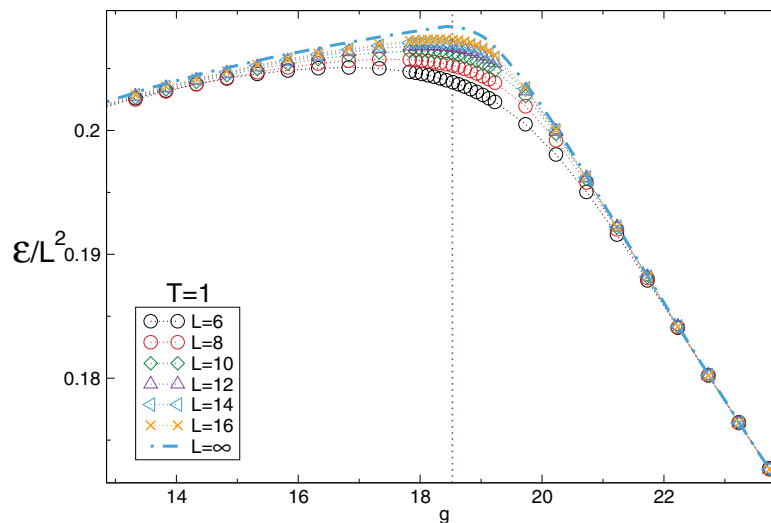


**Figure 17.** Scaling of the negativity $\mathcal{E}$ at a finite-temperature phase transition in the QSM. We plot $\mathcal{E}/L^2$ versus $g$. The results are at fixed $T = 1$. Different symbols are for different sizes $L$. Data are obtained by solving the finite-size constraint equation (20). The vertical dotted line marks the critical point at $g_c \approx 18.52$. The dashed-dotted line is the result in the thermodynamic limit. Note the larger finite-size effects in the critical region.

### 7.1. Entanglement spectra

Let us start discussing the entanglement spectrum. Let us consider the two matrices $\mathbb{Q}_{nm} = \langle s_n s_m \rangle$ and $\mathbb{P}_{nm} = \langle p_n p_m \rangle$ (see section 2). Here we work in the thermodynamic

limit. Since we are interested in the cusp-like singularity of the entanglement spectrum, it is convenient to expand $\mathbb{Q}$ and $\mathbb{P}$ as

$$\mathbb{Q} = \mathbb{Q}_0 + (g - g_c)\mathbb{Q}_1^{\pm} + \ldots \tag{85}$$

$$\mathbb{P} = \mathbb{P}_0 + (g - g_c)\mathbb{P}_1 + \ldots, \tag{86}$$

where the dots denote higher order terms in powers of $g - g_c$, which we neglect. The matrices $\mathbb{Q}_0$ and $\mathbb{P}_0$ are obtained from $S_{nm}^{(0)}$ and $P_{nm}^{(0)}$ (see (80) and (82)), whereas $\mathbb{Q}_1$ and $\mathbb{P}_1$ are easily derived from $S_{nm}^{(1)}$ and $P_{nm}^{(1)}$ (see (81) and (83)). The $\pm$ in $\mathbb{Q}_1^{\pm}$ is to stress that the matrix is different on the two sides of the transition, because of the term $Z_{\text{sing}}$ (see (84)), which is only present for $g > g_c$. We now have at the leading order $\mathcal{O}(g - g_c)$

$$\mathbb{Q} \cdot \mathbb{P} = \mathbb{Q}_0 \cdot \mathbb{P}_0 + (g - g_c)(\mathbb{Q}_0 \cdot \mathbb{P}_1 + \mathbb{Q}_1^{\pm} \cdot \mathbb{P}_0) + \ldots \tag{87}$$

By using standard perturbation theory, one obtains that the corrections to the eigenvalues $\lambda_n^2$ of the matrix $\mathbb{Q}_0 \cdot \mathbb{P}_0$ are given as

$$\delta\lambda_n^2 = (g - g_c)\langle \phi_n | \mathbb{Q}_0 \cdot \mathbb{P}_1 + \mathbb{Q}_1^{\pm} \cdot \mathbb{P}_0 | \phi_n \rangle, \tag{88}$$

where $|\phi_n\rangle$ is the eigenvector of $\mathbb{Q}_0 \cdot \mathbb{P}_0$ corresponding to eigenvalue $\lambda_n^2$. Clearly, the singularity in the negativity is determined by the second term in (88), which depends on $Z_{\text{sing}}$. Now we observe that $Z_{\text{sing}}$ does not depend on the positions $n, m$. This has striking consequences for the single-particle entanglement spectrum. First, the singular contribution in (88) is given as

$$[\delta\lambda_n^2]_{\text{sing}} = (g - g_c)Z_{\text{sing}}\langle \phi_n | (1, 1, \ldots) \otimes (1, 1, \ldots) \cdot \mathbb{P} | \phi_n \rangle. \tag{89}$$

Note that the vector $(1, 1, \ldots) \otimes (1, 1, \ldots) \cdot \mathbb{P} | \phi_n \rangle$ is flat, i.e. all the elements are equal. Moreover, we numerically observed that the eigenvector $|\phi_0\rangle$ is approximately flat, i.e. all its components are $1/\ell^{3/2}$, which reflects the presence of a zero mode. This implies that for $n = 0$ the expectation value in (89) is nonzero. On the other hand, the components of $|\phi_n\rangle$ with $n > 0$ are real and are orthogonal to $|\phi_0\rangle$. This implies that the expectation value in (89) approximately vanishes for $n > 0$. This allows us to conclude that the only few spectrum levels are singular across the transition, i.e. the ones related to the zero mode. We summarize our results in figure 18. The figure shows the single-particle entanglement spectrum levels $\lambda_n^2$. Here subsystem $A$ is the cube of size $\ell$ (see figure 1(c)) embedded in an infinite system. One has that $\lambda_n^2 > 1/4 \, \forall n$. The eigenvalues $\lambda_n^2$ quickly decay with their index $n$. For most of the eigenvalues, one has $\lambda_n^2 \approx 1/4$. In the inset of figure 18 we plot $\delta_n$ defined as

$$\delta_n \equiv (\lambda_n^2)'_+ - (\lambda_n^2)'_-. \tag{90}$$

Here $(\lambda_n^2)'_\pm$ are the right and left derivatives with respect to $g$ of $\lambda_n^2$, calculated at $g_c$. A nonzero value of $\delta_n$ signals that the level $\lambda_n$ is singular across the transition. The results in the figure are obtained by using (89). Clearly, one has that $\delta_n \neq 0$ only for small $n$.
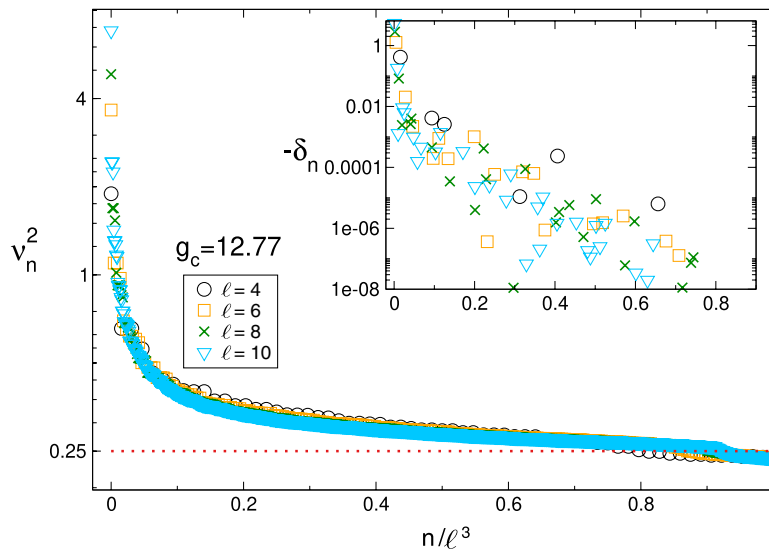
## 7.2. Negativity spectra

We now discuss the negativity spectrum. Subsystem $A$ is now divided into two parts $A_1, A_2$ of sizes $\ell_x = \ell/2, \ell_y = \ell, \ell_z = \ell$ (see figure 1(c)). The partial transposition is
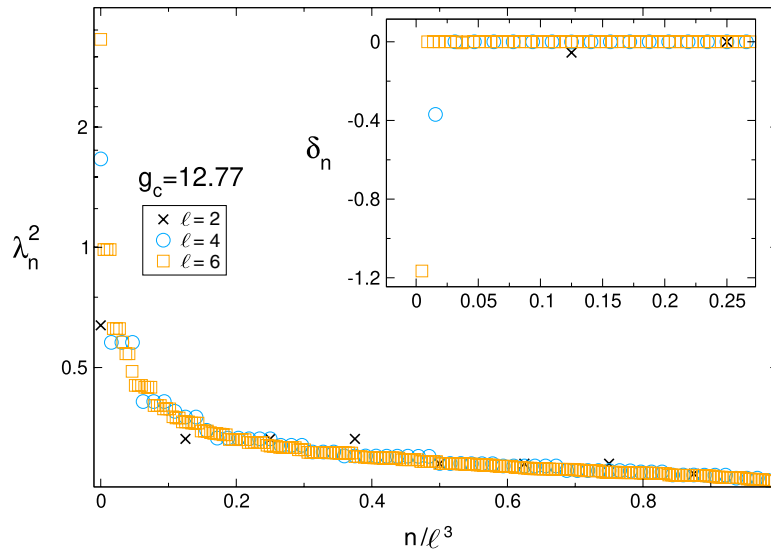
**Figure 18.** Single-particle entanglement spectrum between two adjacent blocks embedded in an infinite system. The figure shows the single-particle entanglement spectrum levels $\lambda_n^2$. The results are at the critical point at $g_c \approx 12.77$. Subsystem $A$ consists of a cube of size $\ell$. Different symbols are for different $\ell$. A logarithmic scale is used on the $y$-axis. Inset: $\delta_n \equiv (\lambda_n^2)'_+ - (\lambda_n^2)'_-$, with $(\lambda_n^2)'_\pm$ the left and right derivative of $\lambda_n^2$ with respect to $g$ calculated at $g_c$. Data are for $\ell = 6$. Note that $\delta_n \neq 0$ only for a small subset of levels.



**Figure 19.** Single-particle negativity spectrum between two adjacent blocks embedded in an infinite system. The figure shows the single-particle negativity spectrum levels $\nu_n^2$. Subsystem $A$ is a cube of size $\ell$. $A_1$ and $A_2$ are the two halves of the cube of linear sizes $\ell_x = \ell/2, \ell_y = \ell, \ell_z = \ell$ (see figure 1(c)). The results are at the critical point at $g_c \approx 12.77$. Note that only the levels $\nu_n^2 < 1/4$ (horizontal dashed line) contribute to the logarithmic negativity. Inset: $\delta_n \equiv (\nu_n^2)'_+ - (\nu_n^2)'_-$, with $(\nu_n^2)'_\pm$ the left and right derivative of $\nu_n^2$ with respect to $g$ at the critical point $g_c$. Note that $\delta_n = 0$ for large $n$, i.e. for the levels that contribute to the negativity.

performed with respect to $A_2$. Our results for the negativity spectrum are shown in figure 19. In the main figure we show the eigenvalues $\nu_n^2$ of the matrix $\mathbb{Q}_0 \cdot \mathbb{P}_0[A^{T_2}]$ versus $n/\ell^3$. For most of the eigenvalues one has that $\nu_n^2 > 1/4$, implying that they do not contribute to the negativity (see section 5.1). As for the entanglement spectrum, the flat vector is an approximate eigenvector of $\mathbb{Q}_0 \cdot \mathbb{P}_0[A^{T_2}]$, with eigenvalue $\nu_0^2$. For instance, we numerically checked that for $\ell = 4, 6$ the eigenvector associated with $\nu_0^2$ has components in the interval $[-0.15, -0.10]$, clustering around the expected value $1/\ell^{3/2} = 0.125$. This behaviour is reflected in that of $\delta_n$. The definition of $\delta_n$ is the same as in (90) after replacing $\lambda_n \to \nu_n$. Clearly, the expansions (85) also hold upon replacing $\mathbb{P}_0 \to \mathbb{P}_0[A^{T_2}]$ and $\mathbb{P}_1 \to \mathbb{P}_1[A^{T_2}]$. For each negativity spectrum level, $\delta_n$ is plotted in the inset in figure 19. In contrast with the entanglement spectrum (compare with figure 18), one has $\delta_n \neq 0$ for a larger subset of levels. For instance, for $\ell = 6$ one has $\delta_n = 0$ only for $n \gtrsim 10$. As it is clear from figure 18 all the levels of the negativity spectrum with $\delta_n \neq 0$ do not contribute to the negativity because they correspond to $\lambda_n^2 > 1/4$. This suggests a suppression of the logarithmic correction to the boundary-law scaling of the logarithmic negativity, in contrast with the entanglement entropy (see section 7.1).

## 8. Conclusions

We investigated the interplay between entanglement and classical fluctuations at finite-temperature critical points. Specifically, we focused on the three dimensional QSM, which has a finite-temperature transition between a paramagnetic phase and a ferromagnetically ordered phase. We considered several entanglement-related observables, such as the von Neumann and Rényi entropies, the mutual information, and the logarithmic negativity. In particular, we characterised the behaviour of the logarithmic negativity in all the different phases and at the transition. We also investigated how the behaviour of the entropies and of the negativity is reflected in the single-particle entanglement spectrum and on the negativity spectrum.

We now mention several important directions for future research. First, it would be important to explore the behaviour of entanglement-related observables in different dimensions. For instance, in $d = 4$ the para-ferro transition becomes mean field. It would be interesting to investigate how this is reflected in the singularity structure of entanglement. An interesting direction is to investigate the logarithmic negativity at the quantum phase transition in $d = 3$. Our results suggest that the logarithmic negativity exhibits a cusp-like singularity. It would be useful to understand how this is reflected in the structure of the negativity spectrum. Another interesting direction is to study the crossover from quantum to classical criticality. Moreover, it would be enlightening to generalize the perturbative analysis developed in section 7 including higher-order corrections. This would allow, in principle, to characterise the full singularity structure of entanglement-related quantities.

It would be also useful to extend our analysis to other entanglement-related quantities, such as the quantum Fisher information, especially in the light of the results of [22]. Interestingly, the QSM remains exactly solvable even in the presence of long-range

interactions. This opens the possibility of studying entanglement-related quantities in long-range models.

Another important direction is to study the out-of-equilibrium dynamics of entanglement-related quantities after a quantum quench. In recent years, it has been shown [101–104] that for integrable models it is possible to describe quantitatively the entanglement dynamics by combining integrability with a quasiparticle picture. It would be interesting to investigate the validity of this picture for $d > 1$. In $d = 3$ this could also allow to investigate whether the presence of finite-temperature criticality affects the entanglement dynamics. Finally, it has been suggested in [105] that in the $O(N)$ model with $N \to \infty$ the steady-state arising after a quantum quench is not described by the so-called Generalized Gibbs Ensemble. The QSM provides an ideal framework to clarify this issue.

## Acknowledgments

## Appendix. Evaluation of some Watson-type integrals

The numerical evaluation of the 3D integrals appearing in the expression for the correlators in (16) is a demanding task. However, there are well-known tricks to reduce them to one-dimensional (1D) integrals. To proceed we imagine of expanding the integrand in (16) in the limit $k \to 0$. Thus, one obtains that the first term is $\propto 1/\omega_k$. The higher-order terms yield integrals of the type $\int \mathrm{d}k/(2\pi)^3 \omega_k^\alpha$, with $\alpha$ a positive integer. These integrals can be performed analytically by exploiting the fact that [106]

$$
\int_{-\pi}^{\pi} \frac{\mathrm{d}k}{(2\pi)^3} \mathrm{e}^{\mathrm{i}kx} \Big( -\sum_{j=x,y,z} \cos k_j \Big)^\alpha
$$
$$
= \begin{cases} 0 & \text{if } \alpha = 0,\ldots,X-1 \\ (-1)^\alpha \alpha! 2^{-|x_1|-|x_2|-|x_3|} \sum_{p_1,p_2,p_3 \geqslant 0} 2^{-2p_1-2p_2-2p_3} \frac{\delta_{p_1+p_2+p_3,(\alpha-X)/2}}{p_1! p_2! p_3! (p_1+|x_1|)! (p_2+|x_2|)! (p_3+|x_3|)!} & \text{if } \alpha - X \geqslant 0, \alpha - X \text{ even.} \end{cases}
$$
(A.1)

Here we defined $X \equiv |x_1| + |x_2| + |x_3|$. Clearly, the integral of $\omega_k^\alpha$ can be obtained by using Equation (A.1) and Newton's binomial formula. We now discuss the integration of the singular contribution. The resulting integral is of the type

$$
\int \frac{\mathrm{d}k}{(2\pi)^3} \mathrm{e}^{\mathrm{i}k(n-m)} \omega_k^{-1}.
$$
(A.2)

The integral (A.2) can be rewritten as a 1D integral. One can use the identity

$$
\frac{1}{1+z} = \int_0^\infty \mathrm{d}t\, \mathrm{e}^{-(z+1)t}.
$$
(A.3)

After using (A.3) in (A.2), the integration over $k$ can be performed explicitly. One obtains

$$\int \frac{\mathrm{d}k}{(2\pi)^3} \frac{\mathrm{e}^{\mathrm{i}k(n-m)}}{\omega_k} = \int_0^\infty \mathrm{d}t \mathrm{e}^{-3t} I_{n_x-m_x}(t) I_{n_y-m_y}(t) I_{n_z-m_z}(t), \tag{A.4}$$

where $I_\alpha(x)$ are the Bessel functions of the first kind. The integral in (A.4) can be efficiently evaluated numerically.

## References

[1] Eisert J, Cramer M and Plenio M B 2010 Colloquium: area laws for the entanglement entropy *Rev. Mod. Phys.* **82** 277
[2] Amico L, Fazio R, Osterloh A and Vedral V 2008 Entanglement in many-body systems *Rev. Mod. Phys.* **80** 517
[3] Calabrese P, Cardy J and Doyon B 2009 Introduction to 'Entanglement entropy in extended quantum systems *J. Phys. A: Math. Theor.* **42** 500301
[4] Laflorencie N 2016 Quantum entanglement in condensed matter systems *Phys. Rep.* **646** 1
[5] Wolf M M 2006 Violation of the entropic area law for fermions *Phys. Rev. Lett.* **96** 010404
[6] Gioev D and Klich I 2006 Entanglement entropy of fermions in any dimension and the Widom conjecture *Phys. Rev. Lett.* **96** 100503
[7] Calabrese P, Mintchev M and Vicari E 2012 Entanglement entropies in free fermion gases for arbitrary dimension *Europhys. Lett.* **97** 20009
[8] Lee J, Kim M S, Park Y J and Lee S 2000 Partial teleportation of entanglement in a noisy environment *J. Mod. Opt.* **47** 2151
    Eisert J and Plenio M B 1999 A comparison of entanglement measures *J. Mod. Opt.* **46** 145
[9] Vidal G and Werner R F 2002 Computable measure of entanglement *Phys. Rev.* A **65** 032314
[10] Plenio M B 2005 Logarithmic negativity: a full entanglement monotone that is not convex *Phys. Rev. Lett.* **95** 090503
    Eisert J 2006 Entanglement in quantum information theory (arXiv:quant-ph/0610253)
[11] Calabrese P, Cardy J and Tonni E 2012 Entanglement negativity in quantum field theory *Phys. Rev. Lett.* **109** 130502
[12] Calabrese P, Cardy J and Tonni E 2015 Finite temperature entanglement negativity in conformal field theory *J. Phys. A: Math. Theor.* **48** 015006
[13] De Nobili C, Coser A and Tonni E 2016 Entanglement negativity in a two dimensional harmonic lattice: area law and corner contributions *J. Stat. Mech.* 083102
[14] Eisler V and Zimboras Z 2016 Entanglement negativity in two-dimensional free lattice models *Phys. Rev.* B **93** 115148
[15] Shapourian H and Ryu S 2018 Finite-temperature entanglement negativity of Fermi surface (arXiv:1807.09808)
[16] Lu T-C and Grover T 2019 Singularity in entanglement negativity across finite-temperature phase transitions *Phys. Rev.* B **99** 075157
[17] Lu T-C and Grover T 2019 Structure of quantum entanglement at a finite temperature critical point (arXiv:1907.01569)
[18] Nandkishore R and Huse D A 2015 Many-body localization and thermalization in quantum statistical mechanics *Ann. Rev. Condens. Matter Phys.* **6** 15
[19] Khemani V, Lim S P, Sheng D N and Huse D 2017 Critical properties of the many-body localization transition *Phys. Rev.* X **7** 021013
[20] Kjall J, Bardarson J and Pollmann F 2014 Many-body localization in a disordered quantum Ising chain *Phys. Rev. Lett.* **113** 107204
[21] Chandran A, Laumann C R and Oganesyan V 2015 Finite size scaling bounds on many-body localized phase transitions (arXiv:1509.04285)
[22] Hauke P, Heyl M, Tagliacozzo L and Zoller P 2016 Measuring multipartite entanglement through dynamic susceptibilities *Nat. Phys.* **12** 778
[23] Gabbrielli M, Smerzi A and Pezzè L 2018 Multipartite entanglement at finite temperature *Sci. Rep.* **8** 15663
[24] Frérot I and Roscilde T 2019 Reconstructing the quantum critical fan of strongly correlated systems using quantum correlations *Nat. Commun.* **10** 577
[25] Melko R, Kallin A B and Hastings M B 2010 Finite-size scaling of mutual information in Monte Carlo simulations: application to the spin-1/2 XXZ model *Phys. Rev.* B **82** 100409

[26] Singh R R P, Hastings M B, Kallin A B and Melko R G 2011 Finite-temperature critical behavior of mutual information *Phys. Rev. Lett.* **106** 135701

[27] Kallin A B, Hyatt K, Singh R R P and Melko R G 2013 Entanglement at a two-dimensional quantum critical point: a numerical linked-cluster expansion study *Phys. Rev. Lett.* **110** 135702

[28] Inglis S and Melko R G 2013 Wang–Landau method for calculating Rényi entropies in finite-temperature quantum Monte Carlo simulations *Phys. Rev.* E **87** 013306

[29] Sriluckshmy P V and Mandal I 2018 Critical scaling of the mutual information in two-dimensional disordered Ising models *J. Stat. Mech.* 043301

[30] Singh R R P, Melko R G and Oitmaa J 2012 Thermodynamic singularities in the entanglement entropy at a two-dimensional quantum critical point *Phys. Rev.* B **86** 075106

[31] Pelissetto A and Vicari E 2002 Critical phenomena and renormalization-group theory *Phys. Rep.* **368** 549

[32] Lu T-C and Grover T 2018 Singularity in entanglement negativity across finite temperature phase transitions (arXiv:1808.04381)

[33] Helmes J and Wessel S 2004 Entanglement entropy scaling in the bilayer Heisenberg spin system *Phys. Rev.* B **89** 245120

[34] Frerot I and Roscilde T 2016 Entanglement entropy across the superfluid-insulator transition: a signature of bosonic criticality *Phys. Rev. Lett.* **116** 190401

[35] Joyce G S 1972 *Phase Transitions and Critical Phenomena* vol 2, ed C Domb and M S Green (New York: Academic) p 375

[36] Brankov I 1996 *Introduction to Finite-Size scaling* (*Leuven Notes In Mathematical And Theoretical Physics; Series A: Mathematical Physics*) (Leuven: Leuven University Press)

[37] Zinn-Justin J 1997 Vector model in the large $N$ limit: a few applications *1998 Lectures at the 11th Taiwan Spring School (Taipei)*

[38] Ruggiero P, Alba V and Calabrese P 2016 Negativity spectrum of one-dimensional conformal field theories *Phys. Rev.* B **94** 195121

[39] Metlitski M and Grover T 2011 Entanglement entropy of systems with spontaneously broken continuous symmetry (arXiv:1112.5166)

[40] Alba V, Haque M and Laeuchli A M 2012 Entanglement spectrum of the two dimensional Bose–Hubbard model *Phys. Rev. Lett.* **110** 260403

[41] Deutsch J M, Li H and Sharma A 2013 Microscopic origin of thermodynamic entropy in isolated systems *Phys. Rev.* E **87** 042135

[42] Santos L F, Polkovnikov A and Rigol M 2012 Weak and strong typicality in quantum systems *Phys. Rev.* E **86** 010102

[43] Kaufman A M, Tai M E, Lukin A, Rispoli M, Schittko R, Preiss P M and Greiner M 2016 Quantum thermalisation through entanglement in an isolated many-body system *Science* **353** 794

[44] Wilms J, Vidal J, Verstraete F and Dusuel S 2012 Finite-temperature mutual information in a simple phase transition *J. Stat. Mech.* P01023

[45] Stéphan J-M, Inglis S and Melko R G 2014 Geometric mutual information at classical critical points *Phys. Rev. Lett.* **112** 127204

[46] Mandal I, Inglis S and Melko R G 2016 Geometrical mutual information at the tricritical point of the two-dimensional Blume–Capel model *J. Stat. Mech.* 073105

[47] Metlitski M, Fuertes C A and Sachdev S 2009 Entanglement entropy in the $O(N)$ model *Phys. Rev.* B **80** 115122

[48] Peres A 1996 Separability criterion for density matrices *Phys. Rev. Lett.* **77** 1413

[49] Zyczkowski K, Horodecki P, Sanpera A and Lewenstein M 1998 Volume of the set of separable states *Phys. Rev.* A **58** 883

[50] Zyczkowski K 1999 Volume of the set of separable states. II *Phys. Rev.* A **60** 3496

[51] Wichterich H, Molina-Vilaplana J and Bose S 2009 Scaling of entanglement between separated blocks in spin chains at criticality *Phys. Rev.* A **80** 010304

[52] Marcovitch S, Retzker A, Plenio M B and Reznik B 2009 Critical and noncritical long-range entanglement in Klein–Gordon fields *Phys. Rev.* A **80** 012325

[53] Wichterich H, Vidal J and Bose S 2010 Universality of the negativity in the Lipkin–Meshkov–Glick model *Phys. Rev.* A **81** 032311

[54] Calabrese P, Cardy J and Tonni E 2013 Entanglement negativity in extended systems: a field theoretical approach *J. Stat. Mech.* P02008

[55] Calabrese P, Tagliacozzo L and Tonni E 2013 Entanglement negativity in the critical Ising chain *J. Stat. Mech.* P05002

[56] Kulaxizi M, Parnachev A and Policastro G 2014 Conformal blocks and negativity at large central charge *J. High Energy Phys.* JHEP09(2014)010

[57] Ruggiero P, Alba V and Calabrese P 2016 Entanglement negativity in random spin chains *Phys. Rev.* B **94** 035152

[58] Rangamani M and Rota M 2014 Comments on entanglement negativity in holographic field theories *J. High Energy Phys.* JHEP10(2014)060

Perlmutter E, Rangamani M and Rota M 2015 Central charges and the sign of entanglement in 4D conformal field theories *Phys. Rev. Lett.* **115** 171601

[59] Blondeau-Fournier O, Castro-Alvaredo O and Doyon B 2016 Universal scaling of the logarithmic negativity in massive quantum field theory *J. Phys. A: Math. Theor.* **49** 125401

[60] Bianchini D and Castro-Alvaredo O A 2016 Branch point twist field correlators in the massive free Boson theory *Nucl. Phys.* B **913** 879

[61] Lee Y A and Vidal G 2013 Entanglement negativity and topological order *Phys. Rev.* A **88** 042318

[62] Castelnovo C 2013 Negativity and topological order in the toric code *Phys. Rev.* A **88** 042319

Castelnovo C 2014 Distilling topological entropy from a single measurement of entanglement on projected systems *Phys. Rev.* A **89** 042333

[63] Hart O and Castelnovo C 2018 Entanglement negativity and sudden death in the toric code at finite temperature *Phys. Rev.* B **97** 144410

[64] Javanmard Y, Trapin D, Bera S, Bardarson J-H and Heyl M 2018 Sharp entanglement thresholds in the logarithmic negativity of disjoint blocks in the transverse-field Ising chain *New J. Phys.* **20** 083032

[65] Bayat A, Bose S, Sodano P and Johannesson H 2012 Entanglement probe of two-impurity Kondo physics in a spin chain *Phys. Rev. Lett.* **109** 066403

Bayat A, Sodano P and Bose S 2010 Negativity as the entanglement measure to probe the Kondo regime in the spin-chain Kondo model *Phys. Rev.* B **81** 064429

[66] Bayat A, Johannesson H, Bose S and Sodano P 2014 An order parameter for impurity systems at quantum criticality *Nat. Commun.* **5** 3784

[67] Alkurtass B, Bayat A, Affleck I, Bose S, Johannesson H, Sodano P, Sorensen E S and Le Hur K 2016 Entanglement structure of the two-channel Kondo model *Phys. Rev.* B **93** 081106

[68] Wen X, Matsura S and Ryu S 2016 Edge theory approach to topological entanglement entropy, mutual information, and entanglement negativity in Chern–Simons theories *Phys. Rev.* B **93** 245140

[69] Wen X, Chang P-Y and Ryu S 2016 Topological entanglement negativity in Chern–Simons theories *J. High Energy Phys.* JHEP09(2016)012

[70] Mbeng G B, Alba V and Calabrese P 2017 *J. Phys. A: Math. Theor.* **50** 194001

[71] Alba V, Calabrese P and Tonni E 2018 Entanglement spectrum degeneracy and Cardy formula in $1 + 1$ dimensional conformal field theories *J. Phys. A: Math. Theor.* **51** 024001

[72] Goldstein M and Sela E 2018 Symmetry-resolved entanglement in many-body systems *Phys. Rev. Lett.* **120** 200602

[73] De Nobili C, Coser A and Tonni E 2015 Entanglement entropy and negativity of disjoint intervals in CFT: some numerical extrapolations *J. Stat. Mech.* P06021

[74] Gray J, Banchi L, Bayat A and Bose S 2017 Measuring entanglement negativity (arXiv:1709.04923)

[75] Cornfeld E, Sela E and Goldstein M 2018 Measuring fermionic entanglement—entropy and negativity (arXiv:1808.04471)

[76] Sherman N E, Devakul T, Hastings M B and Singh R R P 2016 Nonzero-temperature entanglement negativity of quantum spin models: area law, linked cluster expansions, and sudden death *Phys. Rev.* E **93** 022128

[77] Shapourian H, Ruggiero P, Ryu S and Calabrese P 2019 Twisted and untwisted negativity spectrum of free fermions *SciPost Phys.* **7** 037

[78] Turkeshi X, Ruggiero P and Calabrese P 2019 Negativity spectrum in the random singlet phase (arXiv:1910.09571)

[79] Audenaert K, Eisert J, Plenio M B and Werner R F 2002 Entanglement properties of the harmonic chain *Phys. Rev.* A **66** 042327

[80] Eisler V and Zimboras Z 2015 On the partial transpose of fermionic Gaussian states *New J. Phys.* **17** 053048

[81] Coser A, Tonni E and Calabrese P 2015 Partial transpose of two disjoint blocks in XY spin chains *J. Stat. Mech.* P08005

[82] Coser A, Tonni E and Calabrese P 2016 Towards the entanglement negativity of two disjoint intervals for a one dimensional freefermion *J. Stat. Mech.* 033116

Coser A, Tonni E and Calabrese P 2016 Spin structures and entanglement of two disjoint intervals in conformal field theories *J. Stat. Mech.* 053109

[83] Chang P-Y and Wen X 2016 Entanglement negativity in free-fermion systems: an overlap matrix approach *Phys. Rev.* B **93** 195140

[84] Herzog C P and Wang Y 2016 Estimation for entanglement negativity of free fermions *J. Stat. Mech.* 073102

[85] Shapourian H, Shiozaki K and Ryu S 2017 Many-body topological invariants for fermionic symmetry-protected topological phases *Phys. Rev. Lett.* **118** 216402

[86] Shapourian H, Shiozaki K and Ryu S 2017 Partial time-reversal transformation and entanglement negativity in fermionic systems *Phys. Rev.* B **95** 165101

[87] Eisert J, Eisler V and Zimboras Z 2018 Entanglement negativity bounds for fermionic Gaussian states *Phys. Rev.* B **97** 165123

[88] Shiozaki K, Shapourian H and Ryu S 2017 Many-body topological invariants in fermionic symmetry-protected topological phases: cases of point group symmetries *Phys. Rev.* B **95** 205139

[89] Shiozaki K, Shapourian H, Gomi K and Ryu S 2018 Many-body topological invariants for fermionic short-range entangled topological phases protected by antiunitary symmetries *Phys. Rev.* B **98** 035151

[90] Shapourian H and Ryu S 2018 Entanglement negativity of fermions: monotonicity, separability criterion and classification of few-mode states (arXiv:1804.08637)

[91] Henkel M and Hoeger C 1984 Hamiltonian formulation of the spherical model in $d = r + 1$ dimensions *Z. Phys.* B **55** 67–73

[92] Obermair G 1972 *Dynamical Aspects of Critical Phenomena* ed J I Budnick and M P Kawatra (New York: Gordon and Breach) p 137

[93] Berlin T H and Kac M 1952 The spherical model of a ferromagnet *Phys. Rev.* **86** 821

[94] Lewis H W and Wannier G H 1952 Spherical model of a ferromagnet *Phys. Rev.* **88** 682

[95] Vojta T 1996 Quantum version of a spherical model: crossover from quantum to classical critical behaviour *Phys. Rev.* B **53** 710

[96] Wald S and Henkel M 2015 Quantum phase transition in the spin-anisotropic quantum spherical model *J. Stat. Mech.* P07006

[97] Shapiro J and Rudnick J 1986 The fully finite spherical model *J. Stat. Phys.* **43** 51

[98] Guttmann A J 2010 Lattice Green's functions in all dimensions *J. Phys. A: Math. Theor.* **43** 305205

[99] Joyce G S 1998 On the cubic modular transformation and the cubic lattice Green functions *J. Phys. A: Math. Gen.* **31** 5105

[100] Eisler V and Peschel I 2009 Reduced density matrices and entanglement entropy in free lattice models *J. Phys. A: Math. Theor.* **42** 504003

[101] Calabrese P and Cardy J 2005 Evolution of entanglement entropy in one-dimensional systems *J. Stat. Mech.* P04010

[102] Fagotti M and Calabrese P 2008 Evolution of entanglement entropy following a quantum quench: analytic results for the XY chain in a transverse magnetic field *Phys. Rev.* A **78** 10306

[103] Alba V and Calabrese P 2017 Entanglement and thermodynamics after a quantum quench in integrable systems *Proc. Natl Acad. Sci. USA* **114** 7947

[104] Alba V and Calabrese P 2018 Entanglement dynamics after quantum quenches in generic integrable systems *SciPost Phys.* **4** 017

[105] Chandran A, Nanduri A, Gubser S S and Sondhi S L 2013 Equilibration and coarsening in the quantum $O(N)$ model at infinite $N$ *Phys. Rev.* B **88** 024306

[106] Maassarani Z 2000 Series expansions for lattice Green's functions *J. Phys. A: Math. Gen.* **33** 5675